Electrical characterization of hydrogen–vacancy–related defects in monocrystalline silicon

Helge Malmbekk

Thesis submitted in partial fulfillment of the requirements for the degree of Philosophiae Doctor (Ph.D)

University of Oslo, Department of Physics
December 2012

Series of dissertations submitted to the
Faculty of Mathematics and Natural Sciences, University of Oslo
No. 1330

ISSN 1501-7710

Cover: Inger Sandved Anfinsen.
Printed in Norway: AIT Oslo AS.

Produced in co-operation with Akademika publishing.
The thesis is produced by Akademika publishing merely in connection with the thesis defence. Kindly direct all inquiries regarding the thesis to the copyright holder or the unit which grants the doctorate.

Abstract

Electrical characterization of point defects in silicon (Si) is carried out to study fundamental defects present in Si solar cell structures. The interactions between various defect complexes is investigated, while paying special attention to the interactions with hydrogen. As hydrogen is readily incorporated during manufacturing processes, it is important to learn about the defect dynamics of hydrogen related defects

Firstly, hydrogen implantation into *p*- and *n*-type based *pn*-junctions has been investigated in order to learn about the fundamental nature of the defect reactions between vacancy related defects and hydrogen. Samples have been electrically characterized by capacitance–voltage (CV), deep level transient spectroscopy (DLTS) and minority carrier transient spectroscopy (MCTS), which reveals the presence of multiple hydrogen-related levels. A firm correlation between the reported donor and acceptor states of the vacancy–oxygen–hydrogen (VOH) complex is established in *p*-type samples, providing data on formation and annealing of both states. In the *n*-type samples, there is a rapid formation of a hydrogen-related level at $E_c - 0.36$ eV, at the expense of VO, without any formation of VOH after heat treatments at 200 °C. This complex is not observed in the *p*-type samples, leading to the conclusion that the formation barrier for VOH must be higher in *n*-type than in *p*-type material.

Further, an observation of a hydrogen-related defect in *p*-type samples, achieved by MCTS, provides preliminary data that may challenge the accepted model for the di–vacancy–hydrogen complex (V_2H). The level observed in *p*-type samples,

corresponds to a well-known DLTS peak in hydrogen contaminated n-type Si and is often ascribed to the acceptor level of V_2H. However, the theoretically predicted single donor level of V_2H is not observed in the investigated samples, thereby urging additional studies on the validity of the model of V_2H.

Finally, a study of interfaces between tin doped indium oxide (ITO) and silicon has been conducted. Thin films of ITO were sputtered onto crystalline p- and n-type Si wafers, and a lithography process was applied to make individual diodes of various areas. By combining current–voltage (IV), CV and DLTS with secondary ion mass spectrometry (SIMS), a clear understanding of the composition and behavior of the interface is achieved. Heat treatments of the samples up to 600 °C provide information of the defect evolution and the subsequent change in properties of the junction. The ITO/n-Si samples are found to be rectifying at all investigated temperatures, while the ITO/p-Si samples are rectifying up to 400 °C, after which the junctions are transformed into an Ohmic behavior. Correlating these observations with the DLTS measurements reveals that the dominant hole traps anneal out as the rectification of the ITO/p-Si samples is at its highest. Likewise, the annealing of the dominant electron trap is followed by a significant increase in the rectification of the ITO/n-Si samples.

Acknowledgments

First of all I would like to thank my supervisors Prof. Edouard Monakhov, Prof. Bengt Svensson and Dr. Lasse Vines for taking the time to guide me through the work that this thesis has led to. It has been very educational for me to be part of a research group with such quality and experience in the field of semiconductor physics. Your feedback on the countless number of drafts for papers has been valuable for my learning curve in academic writing.

I would also like to thank the research council of Norway for financing the research that has been conducted by myself and the other parts of the Renergi program.

The three years that this thesis has taken of my time, has been a wonderfully educational and interesting period of my life, although quite challenging and frustrating at times. As a PhD-student, one often feel like a particle trapped in an infinite square well, trying to tunnel through the barrier. It is hard to imagine how the thesis would have developed without the generous advice and help from fellow students and employees at the MiNa-lab. The close collaboration with Chi Kwong Tang has been of great value to me. The numerous discussions on semiconductor and DLTS theories over the years, as well as help on the Matlab and Labview programming has taught me a great deal. The friendship, collaboration and discussions with all of the students and employees at MiNa-lab, as well as the solar group at IFE, has been valuable to me and I only hope I have contributed in some ways to your work as well. Last but not least I would like to direct my deepest gratitude towards Victor Bobal for endless assistance in the clean room

lab and for conducting all of the hydrogen implantations needed for my samples.

Finally, I would like to thank my family for always believing in me. Bea, Liv and Signe, you are the light. I love you!

Helge Malmbekk
March 2013

List of included papers

I. **Hydrogen-related defects in boron doped p-type silicon.**
H. Malmbekk, L. Vines, E.V. Monakhov, and B.G. Svensson,
Phyica Status Solidi C 8, No. 3, 705-708 (2011);
doi: 10.1002/pssc.201000260

II. **Hydrogen decoration of vacancy related complexes in hydrogen implanted silicon.**
H. Malmbekk, L. Vines, E.V. Monakhov, and B.G. Svensson,
Solid State Phenomena Vols. 178-179 (2011) pp 192-19;
doi: 10.4028/www.scientific.net/SSP.178-179.192

III. **Comparative study of hydrogen-related defects in p- and n-type silicon.**
H. Malmbekk, L. Vines, B.G. Svensson, and E.V. Monakhov,
In Manuscript

IV. **Annealing dynamics of irradiation-induced defects in high-purity silicon in the presence of hydrogen.**
J. H. Bleka, H. Malmbekk, E.V. Monakhov, B.S. Avset, and B.G. Svensson,
Physical Review B 85, 085210 (2012);
doi: 10.1103/PhysRevB.85.085210

V. **Electronic states at the interface between indium tin oxide and silicon.**
H. Malmbekk, L. Vines, E.V. Monakhov, and B.G. Svensson,
Journal of Applied Physics 110, 074503 (2011);
doi: 10.1063/1.3643002

Contents

Chapter 1

Introduction

Semiconductors are the basis for development of computers, mobile phones and electronics in general since the development of the transistor in the late 1940's. The drive towards smaller, better and more reliable products has lead to an impressive demonstration of the versatility of devices and structures based on a single elemental semiconductor, namely silicon (Si), combined with precise control of impurity levels in the material. The growth of the photo voltaic (PV) industry over the past decade together with the need for radiation hard detectors, e.g. in the Large Hadron Collider [1], has lead to a renewed interest in basic research on defects in Si [2]. Si is pushed to its limits in order to fend off competition from emerging materials and the pursuit for grid parity for the PV industry to be economically competitive to other energy technologies. Whereas most electronics are small size devices produced by the billions per wafer, current main stream PV modules are based on single wafer cells where most manufacturers strive to cut material costs where possible. This has lead to the development of low cost Si wafers where the control of impurities, as well as the crystalline quality, is well below the standard of the electronics industry. This material class is often, somewhat imprecisely, referred to as *solar grade* Si even though the production methods and the resulting material quality differ quite substantially. Accordingly, the interactions between impurities and crystal defects are highly relevant

to the PV industry, but also a highly complex affair as the investigated materials contain multiple components which interact with each other. As such, high quality material is generally a good starting point to investigate defect reactions between various impurities, given that they can be introduced in a controllable and reproducible way.

As the photovoltaic industry grows rapidly, a demand for better and cheaper solar cell structures has lead to an increased attention for heterostructure designs produced by deposition of thin films onto Si wafers. As there are numerous possibilities for structure design, deposition techniques and materials choice, there is a need for fundamental knowledge of interface states between Si and thin films deposited. As tin doped indium oxide (ITO) is a common material applied for transparent conducting purposes in Si technologies, it is vital to learn more about the interface composition as well as the defect states present and the resulting effects on the electrical properties of the structure.

Hydrogen is a common impurity introduced during processing of Si wafers, and it is known that hydrogen interacts with intrinsic defects in Si as well as impurities, by forming new defect complexes where some are electrically inactive. By understanding the basic interactions between hydrogen and the dominant defect complexes in various types of Si materials, cost effective and more reliable devices can be obtained. In most Si wafers the main impurities are carbon and oxygen, which natively do not influence the electronic properties of the material. However, other impurities or vacancy–related defects often generate new defect complexes together with both carbon and oxygen, or by them selves, that do influence the electrical properties. In this work, the interaction between commonly observed defects in Si wafers and hydrogen has been investigated in order to learn more about the fundamentals of hydrogen in Si.

Chapter 2

Basic concepts

2.1 Introduction to semiconductors

A parameter often used to classify materials, is the materials ability to conduct an electrical current. The three main materials classes are then; metals, insulators and semiconductors. The basis for the division, stems from the electronic structure of the material which dictates the conductivity. In single isolated atoms, electrons occupy specific energy levels while in solids, these energy levels form band structures [3]. In semiconductors and insulators, these bands are either completely filled by charge carriers or empty at sufficiently low temperatures and labeled as valence or conduction bands, respectively. Separating the valence and conduction band is the so-called band gap, where no electronic states exist in pure materials, which forms as a consequence of the periodicity of the atoms in the crystal structure. Electrons can be excited over the band gap by thermal energy with the consequence that the excited electron can move in the empty conduction band and that the empty state, ”hole”, left in the valence band can also move. Accordingly, thermally excited charge carriers can lead to conduction in a pure semiconductor. The energy of a band can vary with respect to the electron wave vector $\vec{k}$, with quite intricate shapes and twists, but for this thesis a simplified model where only transitions across the minimum band gap will be

considered. The band gap and thermal excitations of electrons from the valence to the conduction band are schematically shown in Fig. 2.1, where E_g, E_c and E_v are the band gap energy, the energy of an electron at the conduction band edge and the valence band edge, respectively. If an electron is excited from the valence to the conduction band in an ideal intrinsic semiconductor, the amount of holes p in the valence band must equal the amount of electrons n in the conduction band. So for a given temperature:

$$n = p = n_i, \tag{2.1}$$

where n_i is called the intrinsic carrier concentration. A pure semiconductor crystal with no impurities or defects is labeled as intrinsic, although the term is regularly applied also to semiconductors containing impurities but where the conductivity is dominated by thermal excitation of charge carriers across the band gap.

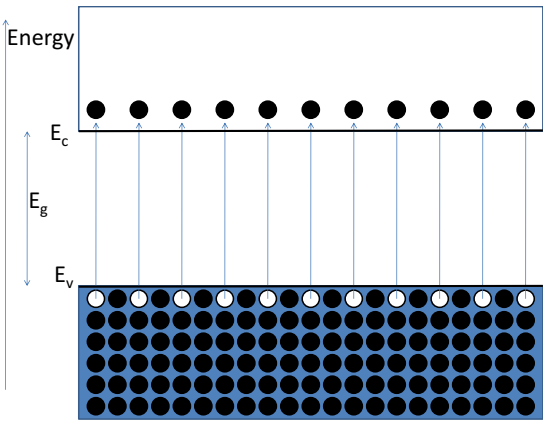

Figure 2.1: Excitation of electrons across the band gap leaving behind empty states (holes)

2.2 Point defects

The conductivity of a semiconductor can be changed by intentionally introducing impurities to the crystal, normally called doping, or by defects. Figure 2.2 shows a schematic view of some types of point defects in crystals. Substitutional defects are foreign atoms occupying a matrix site of the crystal, whereas vacancies represent empty matrix sites. Foreign and host atoms can also occupy various interstitial sites, i.e. non matrix sites. Substitutional atoms that have more valence electrons[1] than the host crystal atoms, can donate their extra electrons to the conduction band (given that the energy level of the extra electron is sufficiently close to the conduction band), whereas substitutional atoms with less valence electrons, can accommodate electrons from the valence band. Thus, impurities can change the population of electrons in the bands. Semiconductors with more electrons in the conduction band than holes in the valence band are called n-type conductors with a doping concentration N_d. More holes in the valence band than electrons in the conduction band makes a p-type conductor with doping concentration N_a. Figure 2.3 illustrates what happens when foreign atoms introduce shallow donor and acceptor states in the band gap.

As electrons are fermions, we have to consider Fermi-Dirac statistics [3, 4] when calculating the concentration of electrons and holes. The concentration of electrons in the conduction band and holes in the valence band are given by:

$$p = \int_0^{E_v} (1 - f(E))N(E)dE \tag{2.2}$$

$$n = \int_{E_c}^{\infty} f(E)N(E)dE, \tag{2.3}$$

where $f(E)$ is the *Fermi-Dirac function* and $N(E)$ is the density of states in the respective bands. $f(E)$ gives the probability that an electron will occupy an electron state of energy E, and can be approximated as

$$f(E) = \frac{1}{1 + e^{(E-E_f)/kT}} \approx e^{-(E-E_f)/kT}, \tag{2.4}$$

[1] Here, valence electrons are defined as the electrons available for chemical bonding.

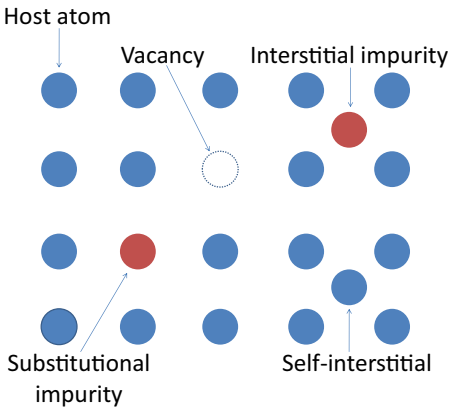

Figure 2.2: Different types of fundamental defects in a 2D elemental crystal structure

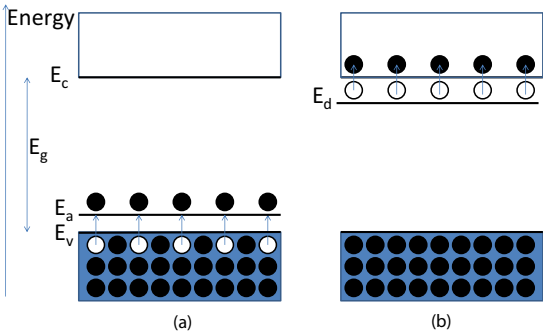

Figure 2.3: a) *p*-type doping. Excitation from valence band to acceptor state b) *n*-type doping. Excitation from donor state to conduction band

where k is Boltzmanns constant, T is absolute temperature and E_f is called the Fermi level, defined so that $f(E_f) = 1/2$. Since $f(E)$ is a step function at 0 K, all levels below E_f are filled and all above are empty. At elevated temperatures, $f(E)$ becomes more smooth and gives a distribution of electrons in the conduction band and holes in the valence band. The approximation of $f(E)$ in Eq.2.4 is valid when E_f is several kT below the conduction band edge E_c, i.e. (E_c-E_f)$\gg$kT, which often holds. Due to the shape of $f(E)$ the states very close to the band edges will be occupied, and we can replace $N(E)$ in Eqs.2.2 and 2.3 with an *effective density of states* ($N_{v,c}$) at the band edges. The concentration of electrons in the conduction band of a doped semiconductor can then be expressed as

$$n = N_d = N_c e^{-(E_c - E_f)/kT}, \tag{2.5}$$

where N_d is the effective donor concentration. The Fermi level will be located close to the conduction band in n-type material at low temperatures, and move towards the middle of the band gap at elevated temperatures. The same holds with respect to the valence band in p-type material.

2.3 Defect states in the band gap

Point defects can introduce states in the band gap, and thereby change the population of charge carriers in the bands. Impurities used for doping should have electronic states close to a band edge in order to maximize the doping efficiency, as a level close to a band edge will require a small amount of thermal energy for ionization. More generally, defects in materials can introduce energy states within the whole band gap. Depending on the energy position of the states, they can have the ability to trap charge carriers, and Fig.2.4 shows a schematic description of the multiple options for capture and emission of charge carriers between an energy state E_t and the bands. For a detailed deduction of the Shockley–Read–Hall statistics [5, 6] that follows, Blood and Orton [7] is recommended.

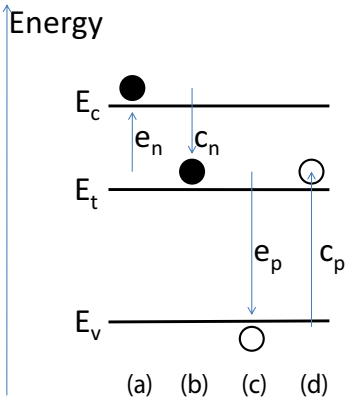

Figure 2.4: The emission and capture processes between an energy level E_t and the bands. a) Emission of electron from the trap b) Capture of electron from the conduction band c) Emission of hole from the trap. d) Capture of hole from the valence band

The capture rate for electrons c_n can be defined as

$$c_n = \sigma_n v_{th,n} n, \tag{2.6}$$

where σ_n is the capture cross section for an electron and $v_{th,n}$ is the thermal velocity of the electron. Further, it can be shown that the emission rate is given by

$$\begin{aligned} e_n &= \sigma_n v_{th,n} N_c e^{-\Delta G/kT} \\ e_n &= \underbrace{e^{-\Delta S/k}\sigma_n}_{\sigma_{na}} v_{th,n} N_c e^{-\Delta H/kT}, \end{aligned} \tag{2.7}$$

where $\Delta G = \Delta H - T\Delta S$ is Gibbs free energy, representing the activation energy of the emission process, ΔH the enthalpy, ΔS the entropy and σ_{na} is called the *apparent capture cross section*. From an experimental point of view, ΔH and σ_{na} can be found from an Arrhenius plot of Eq.2.7 if the temperature independent terms of $v_{th,n}$ and N_c are extracted into a constant β as

$$ln(e_n/T^2) = -\Delta H/kT + ln(\beta\sigma_{na}). \tag{2.8}$$

From a thermal experimental technique, such as DLTS (see Section 3.2), ΔH of the thermal emission process between the trap and the band edges is extracted from the Arrhenius plot, as an average value over the temperature of the measurement. In the literature, however, thermal measurements of ΔH are often sited as $(E_c - \Delta H)$, ignoring the entropy factor (i.e. ΔH is interpreted as ΔG). This is, however, not necessarily valid in all cases, but for deep states in the band gap the difference between ΔG and ΔH is usually assumed to be small. As such, ΔH derived from DLTS measurements is often regarded as the trap signature, rather than the exact energy level. In optical measurement techniques such as photoluminescence, ΔG is always the measured quantity, as the emitted photon is a direct measure of the energy of the transition. It is important to keep this in mind when comparing reported values for energy levels of defects observed with different experimental techniques. For theoretical considerations on the thermodynamics of these processes, Refs.[7, 8, 9, 10] are recommended.

2.4 *pn*-junctions

pn-junctions are essential for many types of semiconductor devices, so a general description will be given in the current section. Let us consider the situation where two semiconductors, one *n*-type and one *p*-type are joined together. The large gradient in charge carriers at the junction will lead to diffusion. When electrons diffuse across the junction, they leave behind positively charged donor-atoms, and holes leave behind negatively charged acceptor-atoms, thereby creating a *space charge region* (W) at the junction (see Fig.2.5). An electric field is set up between the *p*- and *n*-region, opposing the diffusion of charge carriers, as the diffusion current cannot build up forever [4]. In equilibrium, the Fermi levels on both sides must align as the diffusion will balance the drift of charge carriers in the opposite direction. A contact potential (V_0) is developed as a built-in potential barrier for the charge carriers, in order to maintain equilibrium conditions. The potential barrier can be lowered or increased by applying an external bias

(V) to the junction. The electric field sweeps away free charge carriers entering the junction, as such, W is often referred to as a *depletion region*.

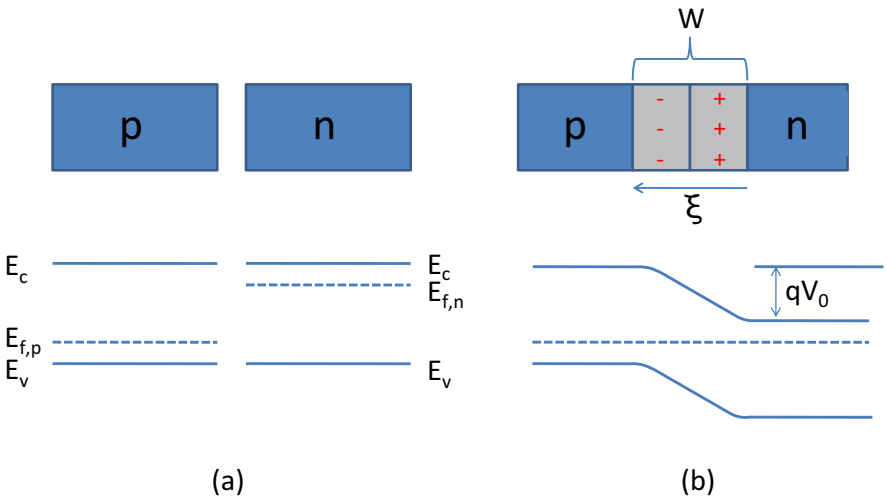

Figure 2.5: a) *p*- and *n*-type semiconductors and their energy bands b) *pn*-junction with the combined energy bands, depletion region, contact potential and electric field

Based on the *Poissons equation* and assuming abrupt transitions of the charge carrier distributions, one can derive an expression for the depletion width as [4]

$$W = \left[\frac{2\epsilon(V_0 - V)}{q}\left(\frac{N_a + N_d}{N_a N_d}\right)\right]^{1/2}, \tag{2.9}$$

where ϵ is the dielectric constant of the material, q is the elemental charge and N_a is the acceptor concentration. The depletion width (W) is a central quantity for the experimental techniques in this thesis, as the junction and its depletion region can be described as a parallel plate capacitor

$$C = \frac{\epsilon A}{W} = \epsilon A\left[\frac{q}{2\epsilon(V_0 - V)}\left(\frac{N_a N_d}{N_a + N_d}\right)\right]^{1/2}, \tag{2.10}$$

where A is the area of the junction cross section. For large differences in doping (e.g. $N_a \gg N_d$), Eq.2.10 simplifies to

$$C = \left[\frac{qN_d \epsilon A^2}{2(V_0 - V)} \right]^{1/2}. \tag{2.11}$$

This equation is the basis for the CV technique, where one can probe the depth profile of the carrier concentration by measuring the capacitance as a function of the applied voltage.

Chapter 3

Experimental techniques

3.1 Capacitance - Voltage measurements

The basis for a capacitance - voltage (CV) measurement is described in Eq.2.11, where the capacitance of a p^+-n junction, can be simplified to

$$C = \left[\frac{qN_d\epsilon A^2}{2(V_0 - V)}\right]^{1/2}.$$

From a measurement of the capacitance vs. reverse bias voltage, the doping concentration in the lowest doped region and the contact potential V_0 of the junction can be deduced by e.g. rearranging Eq.2.11 as

$$\frac{1}{C^2} = \underbrace{-\frac{2}{qN_d\epsilon A^2}}_{a} V + \frac{2}{qN_d\epsilon A^2} V_0, \tag{3.1}$$

where N_d can be found from the slope a, of this linear plot, and V_0 from extrapolating the line to $1/C^2 = 0$ where $V = V_0$.

3.2 Deep Level Transient Spectroscopy

Deep level transient spectroscopy (DLTS) was introduced by Lang in 1974 [11], quickly embraced by Kimerling *et al.*[12, 13, 14, 15, 16], and can give information about electrically active defects and their energy states within the band gap.

From a basic DLTS-scan, the energy position, apparent capture cross section and concentration can be deduced.

3.2.1 Principle of operation

The principle behind DLTS is to charge electrically active defects in the near surface region (depletion region) by changing the externally applied bias voltage. A diode is first kept at a fixed reverse bias, before the bias is removed or changed for typically a few milliseconds (see Fig. 3.1(a)). After the pulse, the reverse bias of the diode is restored, and filled traps start to emit their electrons or holes which are then swept across the junction by the electrical field. The subsequent change in capacitance of the depletion region versus time is measured (see Fig. 3.1(b)). Figure 3.2 shows the band diagram for three situations; steady-state, charging and emission. This is repeated several times for each temperature as the temperature is scanned over a certain range. To ease the analysis as to where the traps are located, an asymmetrically doped *pn*-junction or a Schottky junction are often used, as the depletion region extends primarily into the low doped side of the junction. The DLTS signal is related to the background doping, in the sense that free carriers are needed to fill the traps during the pulse.

3.2.2 The DLTS spectra

A DLTS spectrum can be built by measuring the capacitance of the junction at two fixed times (t_1 and t_2) after the pulse. When the emission rate of a charge carrier from a certain trap is within the range of the measurement interval, a peak in the signal $C(t_1) - C(t_2)$ is obtained. By varying the width of the "time window" defined by t_1 and t_2, a shift in the peak temperature is obtained. More generally and assuming an electron trap, the DLTS spectra $S_i(T)$ can be defined as follows:

$$S_i(T) = \underbrace{\frac{C_{rb}N_t}{2N_d}}_{\Delta C} \underbrace{\frac{1}{n_i}\sum_{t=t_d}^{t_d+t_i} e^{-e_n t} w(t)}_{F_i}, \tag{3.2}$$

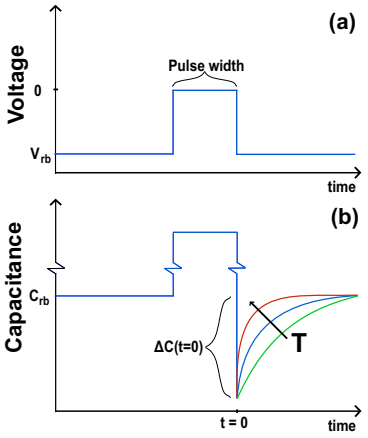

Figure 3.1: (a) The filling pulse. (b) The resulting capacitance changes as a result of the change in bias. The different transients show the effect of higher temperature.

where i is the time window index, C_{rb} is the capacitance at reverse bias, N_t is the density of traps, n_i is the number of measurement points of the transient, t_d is the delay time of the instrumentation and $w(t)$ is a specific weighting function which builds the spectra from the transient. F_i is a numerical parameter related to the length of the time window and the type of the weighting function. By differentiating S_i with respect to T (and e_n), at the top of a DLTS peak, one gets

$$\frac{dS_i}{dT} = \left(\frac{dS_i}{d(e_n t_i)}\right)\left(\frac{d(e_n t_i)}{dT}\right) = 0. \tag{3.3}$$

Hence, numerical values of e_n and F_i can be deduced for each of the specific time windows, by solving $dS/d(e_n t_i) = 0$, as the second parentheses in Eq.3.3 approaches zero only for $T \to 0$ or $T \to \infty$. Values of the emission rate can be plotted versus the peak temperature in Eq.2.8:

$$ln(e_n/T^2) = -\Delta H/kT + ln(\beta\sigma_{na}).$$

Subsequently, ΔH can be obtained from the slope of the Arrhenius plot and σ_{na} from the extrapolated value at $T \to \infty$. The concentration of traps N_t is proportional to the DLTS peak height, according to Eq.3.2.

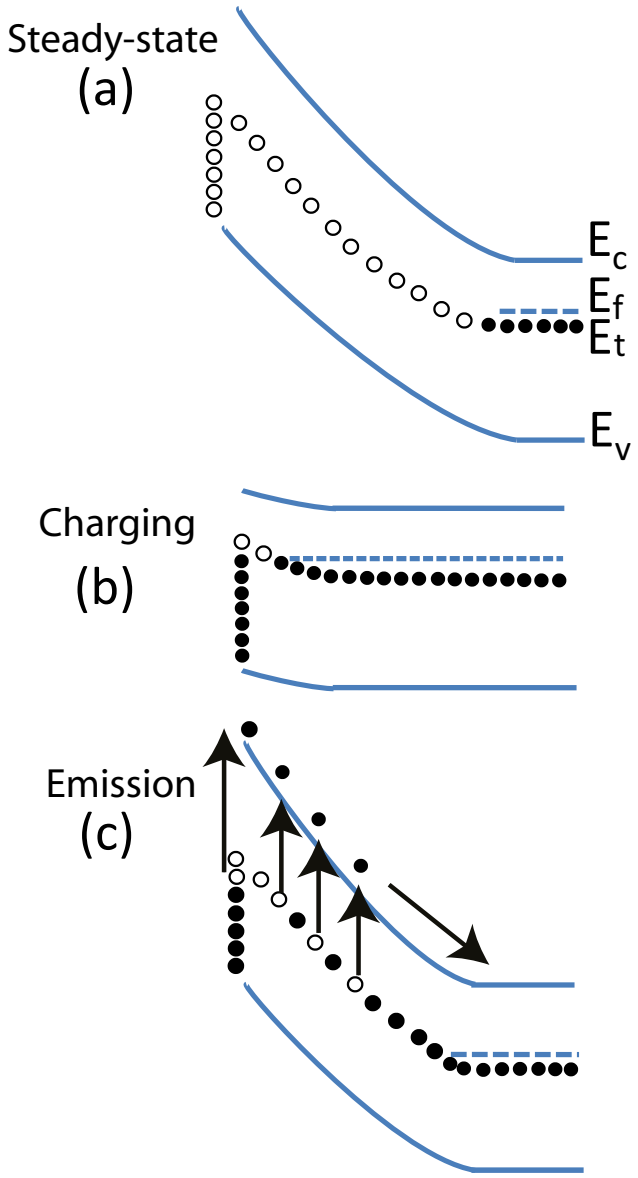

Figure 3.2: Charging and emission of a deep level and interface traps. (a) Steady-state at reverse bias. (b) Charging of traps during pulsing bias. (c) Thermal emission from traps at reverse bias. E_t is the position of a trap in the band gap.

The lock-in and Gaver–Stehfest (GS4) weighting functions [17, 18] have been used in the current work, and a thorough description of these functions and the resulting DLTS spectra, together with numerical values for e_n and F_i, can be found in the PhD theses of D. Åberg [19] and P. Pellegrino [20]. The general idea of the different weighting functions, is that the transient is measured with a fixed time spacing for a certain length, and then a mathematical function $w(t)$ is applied to build different spectra, post measurement. Figure 3.3 illustrates the difference in resolution between lock-in and GS4, where GS4 resolves overlapping peaks better than lock-in, but at the expense of an increased noise level. A trade-off between resolution and noise level has to be made when considering which spectra produce the best description of the data.

In order to separate energy levels with closely overlapping emission properties, Laplace DLTS was developed by Dobaczewski *et al.*,[21] (a commercial software is developed by the authors and co-workers [22]). The technique is based on recording the transient at a fixed temperature and applying an inverse Laplace transformation in order to extract all the components of the decaying exponential. If the measured transient is composed of several closely spaced decaying exponentials, the solution to the inverse transformation is challenging to interpret and in the presence of noise there are no unique solutions. As such, application of the technique requires extensive experience, samples with high signal to noise ratio and combination of several numerical methods for the inverse Laplace transformation.

3.2.3 Profiling

In order to obtain a depth profile of the defects observed by DLTS, a variation in magnitude of the pulse bias can by applied. By stabilizing the temperature at the peak maximum of a specific DLTS signature, and gradually increasing the pulse bias voltage from 0 to $|V_{rb}|$ between each pulse, the region from $W(V_{rb})$ to the surface can be investigated, as shown schematically in Fig. 3.4. In this way,

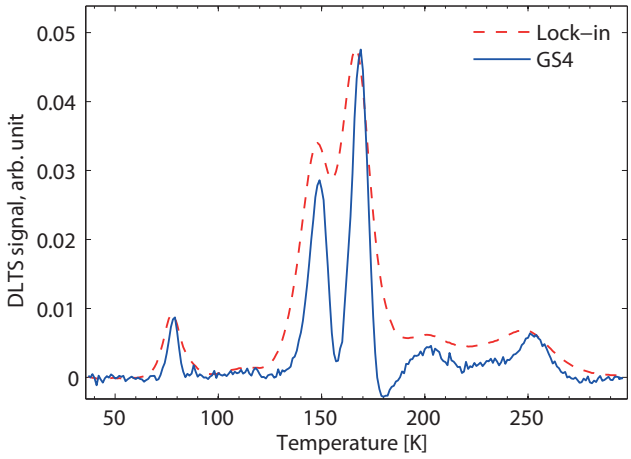

Figure 3.3: DLTS spectra built from the lock-in and GS4 weighting functions. Each peak in the spectra represent an energy level within the band gap.

one starts by probing deep in the bulk, and moves towards the interface of the junction. If the defects are distributed homogeneously in the bulk, the strength of the DLTS signal will increase linearly with depth, unlike in Figure 3.4, where the defects are located in an isolated region of the sample. If a pulse higher than the reverse bias is applied, the diode will go into forward bias during the charging, reducing the depletion region below the built-in one.

3.2.4 Minority Carrier Transient Spectroscopy

DLTS is a majority carrier technique, where majority carriers are injected into the investigated region during the bias pulse, minority carrier transient spectroscopy (MCTS), on the other hand, concerns minority carriers. In Figure 3.5, spectra from DLTS and two different MCTS techniques are compared. In the literature, three different techniques to inject minority carriers are often labelled as MCTS, where in reality only one of these techniques suppresses majority carrier injection. The first technique is based on forward biasing a *pn*-junction during the filling pulse in order to inject minority carriers from the top-surface-near-region of the junc-

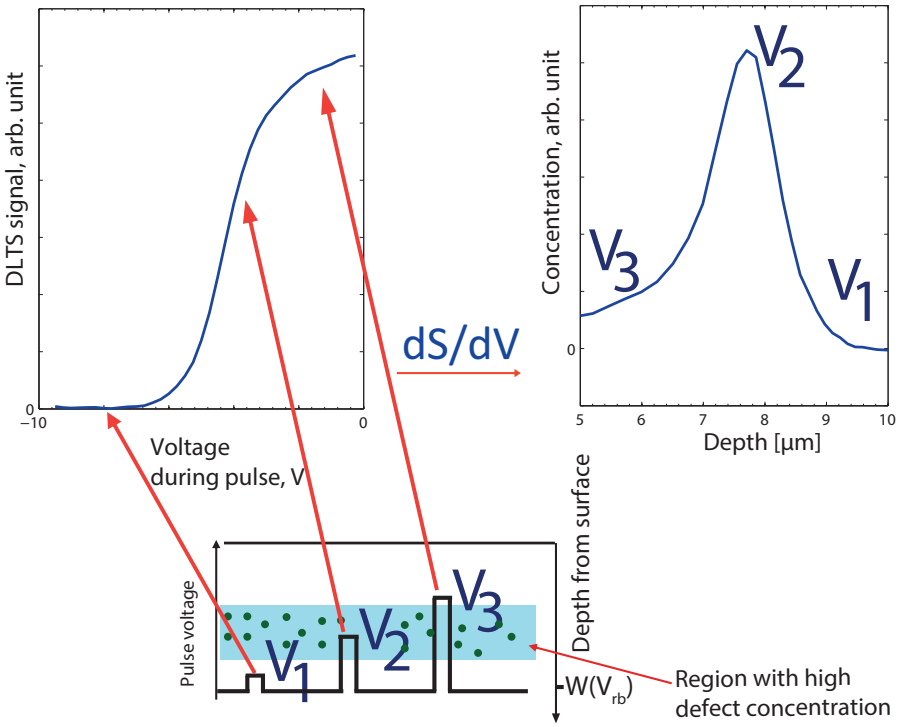

Figure 3.4: Schematic explanation of how the depth profile is obtained.

tion (e.g. the p^+-layer in a p^+n-junction), but this also injects majority carriers from the bulk. As both majority and minority carriers are simultaneously present in the investigated volume, recombination processes might dominate at some defects, as capture of majority carriers might occur with high rates.

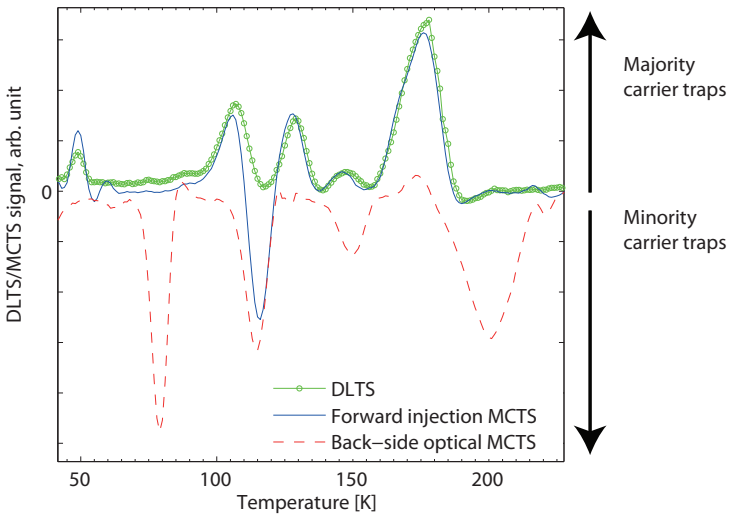

Figure 3.5: Comparison between DLTS, forward injection MCTS and back-side optical MCTS of the same hydrogen implanted sample. Each of the peaks, both positive and negative ones, represent an energy level within the band gap.

The two other techniques are based on optical excitation of electron-hole pairs, where a light source with photon energy larger than the band gap is used to generate the charge carriers. Here, one can choose to shine the light through a semi-transparent diode (Schottky of *pn*-junction), or from the back side of the junction. If the absorption length is shorter than the thickness of the sample, back side excitation will generate charge carriers deep in the bulk and minority carriers will diffuse to the depletion region (assuming the minority carrier lifetime is sufficiently long) while majority carriers are hindered by the electrical field of the junction. In front side excitation, on the other hand, both types of charge carriers will be generated close to the junction and significant contributions from majority

carriers cannot be excluded.

A major advantage of combining DLTS and MCTS, is the correlated information that the techniques can bring for the same samples. When DLTS and MCTS are applied to both n and p-type samples, there is a possibility of determining whether certain types of defects only form in one of the samples. This can lead to a clearer identification of the defect levels investigated. In Figure 3.6(a), DLTS spectra from n-type samples are depicted in the same graph as MCTS spectra from p-type samples, illustrating the types of electron traps which can be detected in both samples ($E1$-$E3$). In Figure 3.6(b), the signatures from hole traps are shown, by comparing DLTS of p-type and MCTS of n-type samples one can determine that $H1$ and $H2$ occur in both sets of samples.

3.3 Secondary Ion Mass Spectrometry

In secondary ion mass spectrometry (SIMS), the investigated sample is bombarded in vacuum by an ion beam (typically Cs^+ or O_2^+), where the incident ions transfer energy and momentum to the atoms of the sample. Some of these atoms will gain enough energy to escape from the sample surface either in neutral or ionized state (shown schematically in Fig. 3.7). The ions can be extracted into a mass spectrometer, where for example electrostatic and magnetic analyzers are used to discriminate between different *mass over charge* (MOC) species. [23]:

$$\frac{m}{q} = \frac{(Br_m)^2}{\xi r_e} \tag{3.4}$$

where m is the mass of the species, B is the magnetic field and $r_{m,(e)}$ are the deflection radius of the two analyzers. In the present work, a Cameca IMS 7F magnetic sector instrument has been used, providing three different types of measurements: i) A complete MOC spectrum is generated by varying the magnetic field systematically, yielding information about the amount of different species in the sample, ii) A depth profile can be obtained by keeping the fields fixed on a certain MOC and relating sputtering time to depth, iii) An image of a certain

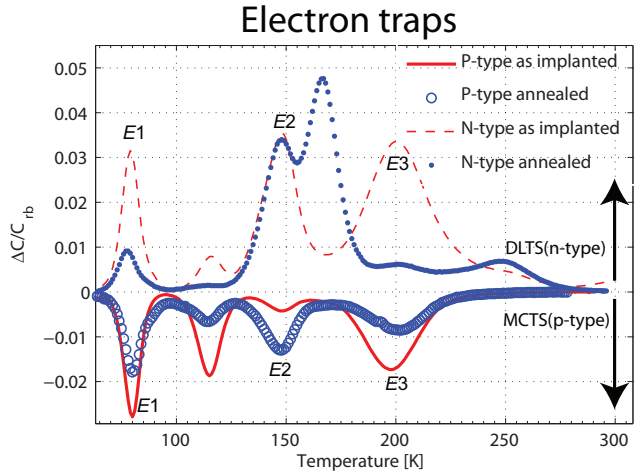

Figure 3.6: Comparison between a) DLTS from n-type sample and MCTS from p-type sample b) DLTS from p-type sample and MCTS from n-type sample. Both sets of samples are implanted with hydrogen.

species is obtained by sweeping a focused incident beam across an area with the fields fixed on a specific MOC.

In order to get quantitative data from SIMS measurements, one often uses reference samples with a known content of specific elements.

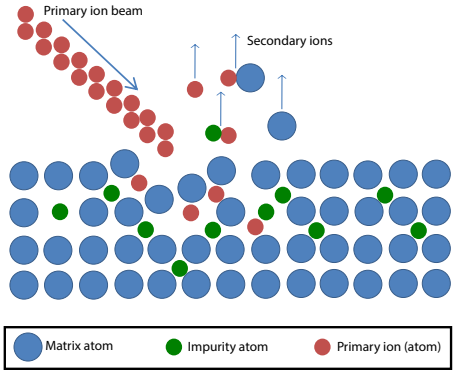

Figure 3.7: Schematic view of how the incident ions transfer energy to atoms in the sample. Some of them will gain enough energy to escape the sample (so-called sputtering).

3.4 Ion implantation

Ion implantation has been widely used for introducing impurity profiles with precise control for many decades. Although the technique did not enter mass production before the mid 1970s [24], Shockley issued a patent already in 1954 with a detailed description of the relevant processes involved [25]. During ion implantation, ionized atoms with well-defined MOC are accelerated by an electrical field and bombard the wafer. By varying the ion energy from a few keV up to several MeV, the projected range of the implanted ions can be varied accordingly, where the absolute values depend on the ion mass. One of the challenging features of ion implantation is the inevitable formation of crystal damage. Although post implantation annealing is normally performed, the heat treatment

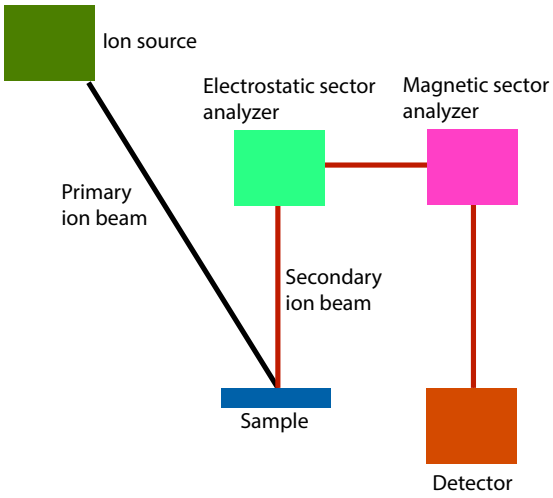

Figure 3.8: Schematic of the SIMS setup in MiNa-Lab at the University of Oslo

will in many cases not fully restore the crystal structure.

The implantation damage, caused by the ions, can also be advantageous for studies of defects in semiconductors, since the defect generation can be controlled by the energy, dose and type of implanted ions. When light elements such as hydrogen are implanted, a measurable amount of point defects can be created with a similar concentration as that of the implanted ions. Accordingly, implantation of hydrogen into Si will generate primary defects which in turn will interact with each other as well as with hydrogen, creating multiple secondary defect complexes where interactions with hydrogen can be studied. Simulated depth profiles for 1 MeV hydrogen implantation in Si with a dose of 10^{10} cm^{-2} is shown in Fig. 3.9. The simulated concentration of vacancies does not take into account dynamic self-annihilation and the actual concentration of vacancies is only a few percent of the depicted values [26, 27]. Complexes of hydrogen and vacancy related defects have been a main focus of this thesis, and controlled implantation of hydrogen has thus been a crucial technique for the studies. For simulations of the implanted depth distribution of hydrogen and the primary defect distribu-

tions, a Monte Carlo based code named TRIM has been applied [28]. As shown in Fig. 3.9, the damage created from an implantation extends all the way from the projected range (∼17 µm) of the implantation to the surface. It it thus possible to investigate defects created by the implantation without influence from the implanted species, if the projected range of the implantation is deeper than the area probed (and the diffusivity of the implanted species is low). Around the projected range of the implantation, on the other hand, interactions between the implanted species and the host crystal damage are enhanced, suitable for investigation.

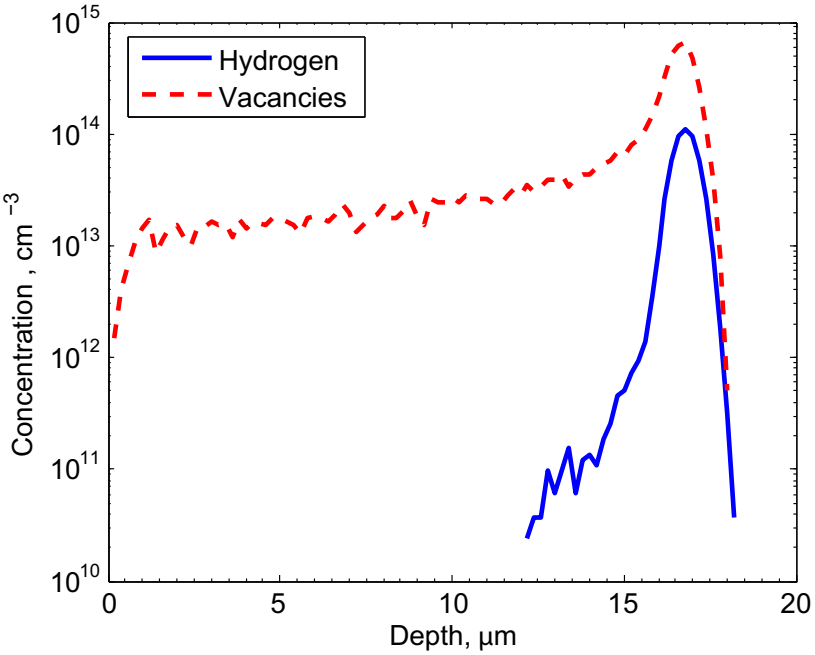

Figure 3.9: Vacancy and hydrogen profiles for a 1 MeV hydrogen implantation in Si with a dose of 10^{10} cm^{-2} simulated with TRIM [28].

Chapter 4

Results and discussions

The following chapter will give a brief review of some of the most relevant literature related to the topics covered in the appended papers, and highlight the motivation for the studies conducted. Finally, a summary of the main results from the thesis will be presented.

4.1 Hydrogen in silicon

Although standard Czochralski (Cz) Si wafers are virtually free of hydrogen, it is a common impurity introduced during semiconductor and solar cell processing, such as chemical etching, polishing, plasma exposure or in–diffusion from thin films deposited on the wafer surface [29]. Incorporation can be either in atomic or molecular form, where the former is the most reactive of the two. It it known, for instance, that atomic hydrogen can electrically passivate dangling bonds around Si vacancies, and thereby create new defect complexes involving both vacancies and hydrogen [30, 31]. As hydrogen reacts with many defects in Si, the diffusion behavior at moderate temperatures is largely influenced by trapping and release at various sites in the crystal, adding to the complexity of the analysis of hydrogen diffusion. Zundel and Weber [32] showed that hydrogen diffusion in boron-doped Si at temperatures between 60 and 140 °C is entirely trap limited,

as hydrogen bonds to substitutional boron to form a boron–hydrogen pair (BH). The formation of BH is clearly observed in the CV measurements in Papers II and III, around the projected range of the implanted hydrogen, as well as near the interface between ITO and *p*-type Si in Paper V. Subsequently, annealing at temperatures around 200 °C leads to a complete dissociation of the BH pair and a corresponding recovery of the electrical activity of boron.

4.2 Defects in particle irradiated silicon

At room temperature, primary defects such as vacancies and self-interstitials migrate readily in a Si crystal and will annihilate, or form more stable complexes with impurities or other primary defects. One of the most common secondary defects observed in Si, post implantation, is the di–vacancy (V_2) [33]. Almost 40 years ago, it was realized that V_2 has three levels in the band gap [15, 34] (and references therein) as shown schematically in Fig. 4.1.

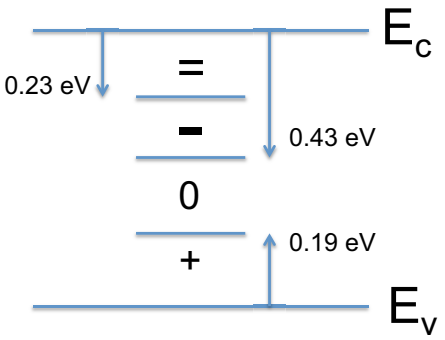

Figure 4.1: Energy levels of the different charge state transitions of the V_2 pair.

As the vacancy diffuses in the Si crystal, it also generates the vacancy–oxygen (VO) complex [35, 36], as well as the vacancy–phosphorus (VP) [37] pair, given that the impurities are present in the sample. The VO complex has an energy level at $E_c - 0.18$ eV while VP has quite recently, compared to its discovery, been shown to possess a second level in the band gap at $E_v + 0.27$ eV, in addition to

the well-known $E_c - 0.45$ eV level [38]. Also quite recently, it has been shown that the tri–vacancy (V_3) has two charge state transitions with energy levels at $E_c - 0.36$ eV and $E_c - 0.46$ eV [39, 40, 41]. Carbon is the second most abundant impurity in Si wafers after oxygen. Si interstitials will migrate and knock carbon out of its substitutional site creating interstitial–carbon (C_i) [42, 43] with energy levels at about $E_v + 0.3$ eV [44] and $E_c - 0.1$ eV [45]. As C_i is mobile at room temperature, it diffuses until it reaches a stable configuration, typically substitutional–carbon interstitial–carbon (C_sC_i) and interstitial–carbon interstitial–oxygen (C_iO_i) are the dominant complexes. C_sC_i has two levels at about $E_v + 0.09$ eV and $E_c - 0.17$ eV [46] while C_iO_i has a level at $E_v + 0.36$ eV [47]. In boron-doped wafers, a dominant minority carrier trap is created after irradiation with an energy level at $E_c - 0.25$ eV, which has been linked with an interstitial–boron interstitial–oxygen (B_iO_i) complex [48], although Vines *et al.* [49] questioned the accepted defect reaction models for the complex and discussed alternative identifications of the level.

4.3 Vacancy–oxygen–hydrogen complexes

The identification of levels associated with hydrogen termination of the *V*O complex, has been a significant part of the work presented in this thesis. As a starting point, the literature on *V*OH levels indicates that there exist a consensus on the identification of a level at $E_c - 0.32$ eV (hereafter labeled $E(0.32)$) as the acceptor level resulting from this complex [50, 51, 52]. Reports have also suggested that a donor state of *V*OH exists at about $E_v + 0.27$ eV (hereafter labeled $H(0.27)$). Historically, this has been founded on the observation by Irmscher [53], that two hydrogen related traps with energy levels at about $E_c - 0.32$ eV and $E_v + 0.27$ eV, possess identical thermal stability and concentration in hydrogen implanted *n*-type samples. Although there are several reports on the $H(0.27)$ level in *p*-type samples [54, 55, 56, 57], data on $E(0.32)$ in *p*-type material are scarce. The paper usually cited [56] in this regard has some shortcomings on the identification of

$E(0.32)$, and the subsequent linking with $H(0.27)$, based on the presented data, is not straight forward. The MCTS spectra presented in Ref.[56] appear to be quite noisy, and the peak attributed to $E(0.32)$ is broader than corresponding peaks from the DLTS spectra. It is also not clear why only parts of the temperature scan is shown for the MCTS spectra, when a much larger temperature range is presented for the DLTS spectra. Hence, a clear identification of $H(0.27)$ is lacking, and detailed annealing studies of the $E(0.32)$ in p-type material are required.

Further, reports from Bleka *et al.*[58] demonstrate that there is a formation of a hydrogen containing VO complex, with an energy level at $E_c - 0.36$ eV (labeled $E(0.36)$), prior to the formation of the ordinary VOH complex in n-type samples. A clear relation between the annealing of VO and the growth of this level was shown at about 200 °C. Accordingly, the level was assigned to a VO complex with a loosely bound hydrogen atom, labeled VOH*. Investigations were undertaken to search for a similar formation of this complex in p-type samples, but only weak indications of a level in the appropriate energy range was observed, which might also originate from the $E4$ level discussed in Section 4.2.

In Papers II and III, a clear observation of $E(0.32)$ was accomplished by utilizing optical MCTS in p-type samples. This level was not observed by forward injection MCTS, as was applied in Paper I. The samples were heat treated up to 300 °C (Paper III), and a clear correlation between $E(0.32)$ and $H(0.27)$ was established for both p- and n-type samples. Both levels were observed after hydrogen implantation, at room temperature, with similar concentration. For the p-type samples, a corresponding growth and annealing behavior was observed after the heat treatments. Further, a close relation between the release of hydrogen from the BH pair and the growth of $E(0.32)$ and $H(0.27)$ was established for the p-type samples, substantiating the relation to hydrogen for the energy levels. For n-type samples implanted with hydrogen, in Papers III and IV, no growth was observed for neither $E(0.32)$ nor $H(0.27)$, before a partial annealing occurred at temperatures above 200 °C. A growth of these levels was only observed during implantation, or during extended annealing at 225 °C of electron irradiated and

hydrogen in–diffused samples (Paper IV). The appearance of $E(0.36)$, formed at the expense of VO in n-type samples, together with the formation of $E(0.32)$ and $H(0.27)$ in p-type samples at temperatures around 125 °C, leads to the conclusion that there is a reaction barrier for VOH formation in n-type samples while the barrier is substantially lower, or non existing, in p-type samples. It is tempting to suggest that the charge state of H plays an important role for the defect reactions occurring. Interstitial (isolated) H is a negative-U center and can be found at tetrahedral (T) site as H^- or H^0 and at bound-centered (BC) site as H^0 or H^+ [59]. In equilibrium, it is characterized by a $(+/-)$ level just above the middle of the bandgap and the charge state changes involve transition between the T- and BC-site. H^- is likely to dominate in the n-type samples which favors formation of the $E(0.36)$ center, possibly via a mechanism invoking the transition from T- to BC-site, on the expense of VOH. In the p-type samples, H^+ prevails during annealing and VOH forms readily without any barrier, whilst $E(0.36)$ is strongly suppressed.

In Paper IV a defect reaction model is presented, explaining the hydrogen mediated transformation of VO into VOH*, back to VO and then into VOH and VOH_2 after extended annealing.

4.4 Vacancy–hydrogen complexes

Substantial efforts have been taken to provide experimental data which contribute to the identification of the different vacancy–hydrogen related complexes in Si. The task is, however, not trivial as there generally exist multiple complexes in the same samples with somewhat similar properties. As there are few theoretical papers on the energy levels from these complexes, further simulation work could aid the understanding of the observed levels from DLTS and MCTS. Some works have indicated that the hydrogen terminated dangling bonds around Si vacancies induce similar energy levels in the band gap regardless of whether there are one or two vacancies in the complex, leading to overlap between different energy

levels in the DLTS spectra (see for instance [50]). Based on simulation work of the electron density around $V\mathrm{H_n}$ complexes, Jones *et al.*[60] argued that VH should posses both an acceptor and a donor level within the band gap, and that the addition of another hydrogen will leave the center with only an acceptor level. Similar results, and considerations, were presented in the work by Coutinho *et al.*[61], where the position of the energy levels of V_2H and $V_2\mathrm{H_2}$ were calculated. Papers I, II and III in the thesis investigate the hydrogen passivation of V_2 by monitoring the annealing of the defect levels observed after hydrogen implantation and subsequent heat treatments. In Paper I, a connection between the annealing of V_2 and the growth of a hydrogen related level, $H(0.25)$, was observed. This connection was, however, dismissed by further investigations in Paper II by observing that the growth of $H(0.27)$ (labelled $H(0.25)$ in Paper I) occurs at temperatures where V_2 is stable.

By combining DLTS and optical MCTS in Paper II (p-type samples) and Paper III (p- and n-type samples), a more complete understanding of the energy levels was obtained. When studying defects which are present in both n- and p-type material (i.e. not related to the dopants), it is beneficial to apply both DLTS and MCTS in order to gain as much information about the defect levels as possible. As the capture cross section for holes and electrons can differ by many orders of magnitude for some defect levels, the probability for recombination, rather than trapping, might hinder the detection of certain levels when only considering one conduction-type of sample. The effect can be minimized by applying back side optical MCTS, as opposed to front side MCTS or forward injection MCTS (see Section 3.2.4). The difference between forward injection MCTS (Paper I) and optical MCTS (Paper II and III) is striking for the investigated samples. By applying optical MCTS, a total suppression of majority carrier traps was achieved, leading to the observation of multiple minority carrier levels which were not resolved by the forward injection MCTS in Paper I. The measurements were achieved by pulsing an infra-red light emitting diode from the back side of the sample, while keeping a fixed revers bias.

The application of optical MCTS leads to the detection of a level at $E_c - 0.45$ eV, labelled $E(0.45)_p$, in the p-type samples, with a concentration significantly higher than expected if resulting from $V_2(-/0)$ alone. A correlation between $E(0.45)_p$ and the $E(0.43)_n$ level, observed in the n-type samples, was revealed in Paper III based on similar thermal stability and rate of electron emission. In order to strengthen the connection between these levels, both peaks are compared in Fig. 4.2. Here, the DLTS and MCTS peaks from hydrogen implanted n- and p-type samples are compared with simulated spectra consisting of four different levels ($S1$-$S4$), as the experimental peaks are quite broad. The close fit between the simulation and the experimental data, as compared to the simulation of a single level, supports the notion that both $E(0.43)_n$ and $E(0.45)_p$ contain multiple levels. Even though the extracted peak properties are not identical, it is likely that they are resulting from the same levels. A slight shift in the peak position can be generated by a difference in concentration between the components of the peak.

The simulated values for $S1$-$S4$ were defined in the following way: $S1$ was based on the peak values from $E(0.43)_n$, $S2$ was based on the expected values of $V_2(-/0)$ with the same peak height as $V_2(=/-)$ in the same sample, $S3$ was based on the peak seen at about 215 K in Fig.4(b) in Paper III and $S4$ was added to get a close correlation between the experimental and simulated spectra. The parameters associated with the simulated peaks are not in any way a unique solution to the simulated curve, but the simulation fit for up to six different rate windows simultaneously. Here, it is important to note that the acceptor level of the vacancy–phosphorus (VP) complex is usually found to overlap with $V_2(-/0)$ in n-type samples. However, the donor level of VP[38] is not observed in the studied n-type samples and the contribution from this level is thereby expected to be minor.

In this regard, Paper III discusses what these results would mean for the generally accepted model of the V_2H complex, namely that there exist some contradictions in the arguments linking $E(0.43)_n$ to V_2H when the results from p-type samples are taken into considerations. From this model, one would expect that

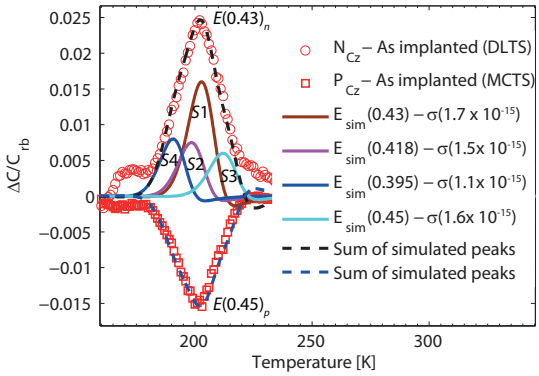

Figure 4.2: DLTS (positive signal) and MCTS (negative signal) spectra of hydrogen implanted n and p-type Si (Rate window (640 ms)$^{-1}$ - GS4) compared with simulated DLTS/MCTS peaks. Units for the simulated energy levels are $E_c -$ eV for energy position and cm^2 for the capture cross section.

the peaks from $V_2(-/0) + V_2\mathrm{H}(-/0)$ and $V_2(0/+) + V_2\mathrm{H}(0/+)$ were identical when observed in the same samples. However, the data presented in Paper III, indicate that $E(0.45)_p$ is about twice the peak height of $V_2(0/+)$ (which should overlap with $V_2\mathrm{H}(0/+)$). Accordingly, the data presented in Papers II and III add interesting perspectives to the ongoing work in identifying the energy levels related to various vacancy–hydrogen complexes. In fact, a complete separation of the levels responsible for the DLTS peaks overlapping with the V_2 levels would increase the understanding of the structure of the energy levels resulting from the hydrogen terminated vacancy complexes.

4.5 Light induced degradation

A topic that has been investigated, but not discussed extensively in the appended papers, is the search for the defect responsible for the so–called *Light Induced Degradation* (LID) of Si solar cells. It is generally observed that solar cells, based on boron doped Si wafers, show a a few percent relative degradation of the

efficiency after a few days in sunlight. Even high efficiency solar cells based on monocrystalline Cz wafers, where metal contaminations are very low, have shown a 10% relative efficiency drop [62] (and references therein). The efficiency can, however, be restored after a 30 min heat treatment at about 200 °C in the dark. Many studies on the topic have pointed to a drop in the lifetime of minority carriers after exposure to sunlight, and the working hypothesis is that a defect complex related to boron and oxygen is responsible for the increased recombination activity. Based on lifetime measurements a substitutional–boron oxygen dimer (B_sO_{2i}) was suggested as the structure of the defect complex [62, 63]. The formation of the complex was proposed to originate from fast diffusing oxygen dimers [63], but this diffusion mechanism has recently been questioned by Murin *et al.*[64]. Macdonald *et al.*[65] presented results that indicated that the concentration of the defect is proportional to the net hole concentration and not to the B_s concentration. This lead Voronkov and Falster [66] to propose an interstitial–boron oxygen dimer (B_iO_{2i}) as the structure of the defect, but this structure was dismissed by Carvalho *et al.*[67] based on theoretical predictions of both the energy levels resulting from the complex and the concentration of B_i.

Although theoretical work suggests that the defects should be possible to detect by DLTS techniques no such observation has been published. In the course of this thesis, substantial efforts have been taken in order to search for this defect complex, but without success. The defect has escaped detection by standard DLTS of boron doped Si wafers with a doping concentration in the range of $10^{14} - 10^{16}$ cm^{-3} both before and after exposure to a solar simulator (Newport 91160 Full Spectrum Solar Simulator) producing radiation equivalent of about one sun for up to 24 h. Samples have been investigated by DLTS, optical MCTS and forward injection MCTS without any clear indications of the defect complex in question. As these studies were unfruitful, samples were prepared in order to convert the *p*-type conductivity of the boron doped wafers into *n*-type by introducing thermal donors [68] (and references therein). This was done in order to conduct standard DLTS in search for electron traps in the top part of the band

gap, as DLTS generally has a higher detection sensitivity than MCTS techniques. Hence, boron doped Si wafers ($[B_s] \approx 10^{15}$ cm^{-3}) were thermally annealed in a tube furnace at 450 °C for about two days, leading to an effective *n*-type carrier concentration of about 10^{15} cm^{-3}. After the thermal treatment, Schottky barrier diodes were formed by thermal evaporation of gold. During the thermal evaporation, the samples were exposed to a bright light source resulting from resistive heating of the crucible for a few minutes. Figure 4.3 shows the DLTS spectra obtained after the samples were prepared. A clear peak can be observed, with an energy position of about $E_c - 0.35$ eV, which is in the expected range of the LID defect. The samples were then exposed to radiation from the solar simulator for 16 h, but no change was observed in the DLTS spectrum. A heat treatment at 250 °C was then conducted, leading to a loss of the peak. Subsequent light soaking for 23 h lead to a broad peak in the DLTS spectrum in Fig. 4.3, which cannot be directly linked to the peak observed prior to the heat treatment. Both spectra show a marked base line shift, which complicates the analysis of the defect concentration. Still, the experiments show that the technique of converting the *p*-type wafers into *n*-type conductivity leads to a detection of possible candidates for the LID defect with concentrations four orders of magnitude below the carrier concentration. A possible follow-up of the current study, could thus be to prepare thermally inverted *p*-type wafers with an *n*-type effective carrier (electron) concentration around 10^{13} cm^{-3}, thereby increasing the possibility of detecting low concentration defects. This was explored, but the Schottky barrier diodes formed on these high resistivity samples had too high leakage current for reliable DLTS measurements.

4.6 Interface defects between indium tin oxide and Si

The prospect of producing low-cost Schottky type solar cells is based on the deposition of a low cost transparent conducting oxide onto a Si wafer. In Paper V, a study of tin doped indium oxide (ITO)/Si interfaces, is conducted, in an at-

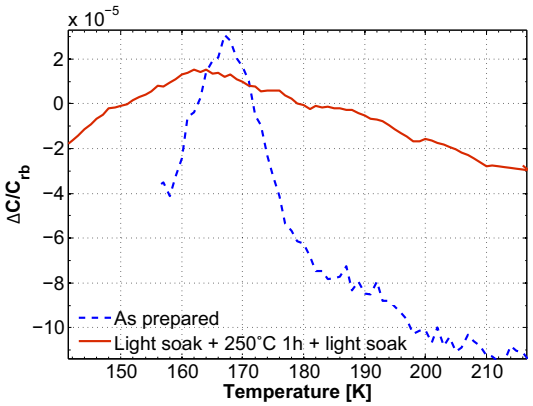

Figure 4.3: DLTS spectra of thermal donor compensated p-type samples exposed to light soaking and heat treatments at 250 °C. Rate window $(640\ \text{ms})^{-1}$ - Lock-in.

tempt to understand the nature of the interface properties that govern the current flow across the junction. Accordingly, the main focus was to learn about the fundamental nature of defects formed at the interface during deposition of ITO, at what point the defects would anneal out, and how the resulting interface properties were affected.

Thin films of ITO were sputtered onto n- and p-type Si wafers (Paper V), and subsequently analyzed by current - voltage (IV), CV, DLTS, SIMS and four point probe measurement techniques after various post deposition heat treatments. If deposited at room temperature, ITO films posses a high resistivity and heat treatments around $300 - 400$ °C are required in order to improve the conductivity of the films [69, 70, 71, 72]. The same general result was observed in Paper V, where the deposited films experienced a drop in resistivity by an order of magnitude after heat treatments in the range of $250 - 450$ °C.

It was realized early on that the ITO/n-Si samples exhibited the highest rectification, as compared to the ITO/p-Si samples, with a significant increase after heat treatments at 450 °C. The ITO/p-Si samples were shown to have their

highest rectification after heat treatments at $250 - 300$ °C, while increasing the temperature to around $400 - 450$ °C lead to a complete loss of the rectifying behavior, thus producing an Ohmic contact between ITO and *p*-type Si. In order to probe the interface of the junction by DLTS, a forward bias voltage was applied during the filling pulse. As there is a build–in depletion region around the junction interface, at zero voltage, applying a forward bias ensures that the extent of this region is minimal during the filling pulse. Thus, defects located close to the interface are possible to detect. Since the samples are Schottky junctions, minority carriers are, however, generally not injected into Si during the pulse as would be the case of a *pn*-junction (see Section 3.2.4) and minority carrier levels were not possible to detect.

The IV and DLTS measurements of the samples revealed a clear correlation between the rectifying behavior of the junctions and the defects present at the interface. Accordingly, a loss of the dominant hole and electron traps produced an increase in the rectification of the ITO/*p*-Si and ITO/*n*-Si samples, respectively. The annealing of the dominant electron trap, which was also correlated with the loss of rectification of the ITO/*p*-Si samples, indicates that the electron traps are involved in the formation of the barrier at the ITO/*p*-Si junction. Further, the observed hole traps were shown to have point like nature, while the electron traps appeared to consist of multiple overlapping energy levels. In the latter case, the DLTS peaks were quite broad and the corresponding emission showed a non linear behavior when depicted in an Arrhenius plot.

From the SIMS measurements, it was evident that significant concentrations of carbon and hydrogen were present at the interface. After heat treatments, a loss of hydrogen was observed, where the most significant drop occurred after 400 °C. Correlating the SIMS data with CV data, indicated that the initial drop in carrier concentration around the ITO/*p*-Si interface is due to formation of BH pairs. The release of hydrogen from this complex, is identified as the cause of hydrogen passivation of the dominante hole trap, H(0.37), while the loss of hydrogen at 400 °C, might be due to a breakup of hydrogen passivated complexes

and a subsequent out–diffusion of hydrogen from the interface region.

Chapter 5

Concluding remarks and future work

The focus of this thesis has been on hydrogen related defects in Si structures. The fact that hydrogen is easily adsorbed on surfaces and readily incorporated at interfaces, during device processing, necessitates a model describing which defect complexes exist at a given temperature for various process steps. As the fundamental understanding of passivation of defect complexes is incomplete, substantial efforts were devoted to identifying commonly observed hydrogen related defects. Two of the most abundant implantation-induced defects in Si, are the V_2 and VO complexes. There are, however, questions yet to be answered about the formation of hydrogen terminated dangling bonds around these complexes, where the formation of VOH and V_2H is still under debate.

In this regard, we have observed an energy level, $E(0.45)_p$, in the hydrogen implanted p-type samples (Papers II and III). The level position is in the range of that usually reported, from measurements of n-type Si, as the first acceptor level of the di–vacancy–hydrogen complex ($V_2\mathrm{H}(-/0)$). The deduced concentration of this level, from the p-type samples, compared to the concentration of the donor level of V_2, casts doubt on the assignment of a donor level for V_2H and/or the identification of the presumed $V_2\mathrm{H}(-/0)$ level.

Another contribution of this thesis, has been the detection of an energy level at $E_\mathrm{c} - 0.32$ eV by MCTS in p-type samples, and a demonstrated one-to-one correla-

tion with an energy level at $E_v + 0.27$ eV. Both levels are commonly observed in *n*- and *p*-type samples, respectively, but a systematic investigation of both levels by DLTS and MCTS of both *n*- and *p*-type Si demonstrate the strength of combining these techniques when drawing conclusions on identification of defect levels. Further, the formation of another hydrogen related *V*O level (*V*OH*), has been studied by both in–diffusion and implantation of hydrogen together with a model describing the formation and subsequent transformation into the more stable *V*OH and VOH_2 complexes. An interesting observation in this regard, is the lack of formation of *V*OH* in the *p*-type samples investigated. The conclusions drawn, point to the existence of a barrier for *V*OH formation in *n*-type as compared to *p*-type samples, where *V*OH grows rapidly within minutes at 125 °C. The formation of *V*OH*, in the *n*-type samples, could be related to the charge state and configuration of H, as it is expected to change from H^- to H^+, by hopping between the BC-site and the neutral charge state at the T-site, at 200 °C.

Si is a well studied material, and a good candidate for combining theoretical and experimental studies. Calculations of energy levels resulting from various defect complexes are improving every year, as the computational methods develop. In this regard, it would be very interesting and helpful with more computational work done on the energy levels from defects containing dangling Si bonds.

A hot topic, and sometimes frustrating, is the lack of experimental observation of the defect responsible for light induced degradation of Si solar cells. If the degradation is related to a specific defect, it should be possible to detect experimentally, either in an enriched form or in common Si wafers. One possible way to increase the capability to detect the defect, is to engineer a sample where the effective carrier concentration is quite low (around $10^{12} - 10^{13}$ cm^{-3}), either by co-doping with both phosphorus and boron, or by introducing thermal donors to a highly boron doped wafer. In this way, one could possibly increase the concentration of the LID defect relative to the carrier concentration and thereby increase the detectability by DLTS and MCTS. The introduction of thermal donors might,

however, influence the formation of the LID defect as the formation of both these types of defects are related to the oxygen content. Nevertheless, an observation of the defect by electrical techniques such as DLTS is highly desirable and should be given a fresh look by anyone with good ideas as to how the defect can be elucidated.

Appendix A

Pn-junction fabrication

The following sections will describe the relevant processes involved in the fabrication of the *pn*-junctions that were used in the experimental work of this thesis, schematically shown in Fig. A.1.

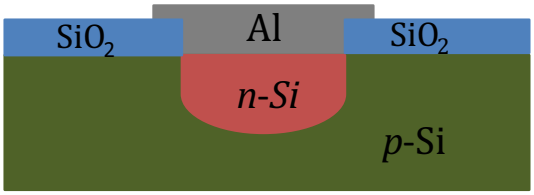

Figure A.1: Finished structure

A.1 Oxidation

Prior to oxidation, the wafers were cleaned with a standard RCA etch procedure in three steps:

- RCA 1 – 5:1:1 of H_2O:NaOH:H_2O_2
- RCA 2 – 50:1 of H_2O:HF
- RCA 3 – 5:1:1 of H_2O:HCl:H_2O_2

$10 - 15$ min can be used for RCA 1 and 3, and about 10 s in RCA 2. When applying RCA 2 to a Si wafer, one should wait until the surface shows hydrophobic behaviour before finishing, as this is a clear test to show that the oxide is completely etched away. DI-water is used to rinse the wafers between each step, and it is important to remember to heat the RCA 1 and 3 solutions to about 75 °C, or else the cleaning will not be very efficient. After the wafers are clean and dry, a 3 h dry oxidation with O_2 flow at about 1100 °C gives about 250 nm SiO_2. The gas should be turned on $10 - 15$ min before loading the wafers in order to establish steady-state and uniform conditions. An N_2-flush before removing the wafers might lead to a better oxide interface, according to literature, but no significant differences were observed. Wet oxidation is supposed to work even better for passivation, but this is not done in our lab at the moment.

A.2 Etching holes in silicon dioxide

The oxide on the back of the wafer, can be kept as a protective layer during the diffusion, to ensure that no dopants enter the backside. If implantation is used, the oxide at the back is not needed. To protect the oxide, photoresist is spin coated on the backside and hard baked at 120 °C for about 15 min. Standard positive photolitography process is then used to open holes for an oxide etch. Mask 1, shown in Fig. A.2(a), is used with 300 W exposure for 30 s. These values might not be optimized, but work fine. The developer solution needs to be 1:4 of Dev:H_2O or more concentrated. Additional developer might be needed if several wafers are developed in a row. Complete developing might take as long as $10 - 20$ min some times, dependent on how efficient the exposure has been. Inspection can be made by an optical microscope to see if the development is completed. There should be a high contrast between the remaining photoresist and the exposed oxide. When the photoresist is completely removed under the exposed regions, a buffered oxide etch (BOE) is used to open the holes in the oxide. The etch rate is about $50 - 100$ nm/min at room temperature. As the backside is covered by pho-

toresist, it might be wise to test the etch rate on a similar sample of equal oxide thickness to ensure that the etching time is long enough. The photoresist should not be affected by the etch when using BOE, but diluted HF will consume even the unexposed photoresist in a few minutes. Importantly, HF solutions are very hazardous and plastic containers and tweezers need to be used. When the oxide etch is complete, most of the photoresist can be removed by rinsing in acetone for a few minutes. As the primer and some residual photoresist are hard to remove by RCA 1, a Piranha etch is used to remove organics on the wafer surface.

- Piranha etch consists of 3:1 of H_2SO_4:H_2O_2.

It is important to be careful when preparing this solution, as the chemicals generate a lot of heat and fume when mixed. When small amounts are used, the mixing order does not really matter. Metal tweezers must be used in this solution as it burns everything that is organic within a few seconds. To finish this part, a cleaning in RCA 1-3 is applied. The wafers should now be put in an appropriate clean container for transport to a diffusion furnace or ion implanter.

A.3 Implantation or in-diffusion

To produce an emitter, one can either use a controlled in–diffusion in a furnace dedicated to emitter formation, or ion implantation and subsequent activation in a tube furnace or by rapid thermal processing. In this work, an in–diffusion from gas face in a commercial tube furnace has been applied.

A.4 Contacting

In order to improve the electrical contact between the diode and a probe needle, an Ohmic contact is formed by evaporation of Al over the oxide opening, thereby capping the hole with a metal as well. Cleaning the wafers is done by RCA 1-3, with a bit longer time on RCA 2 than usual (about 30 s) in order to completely

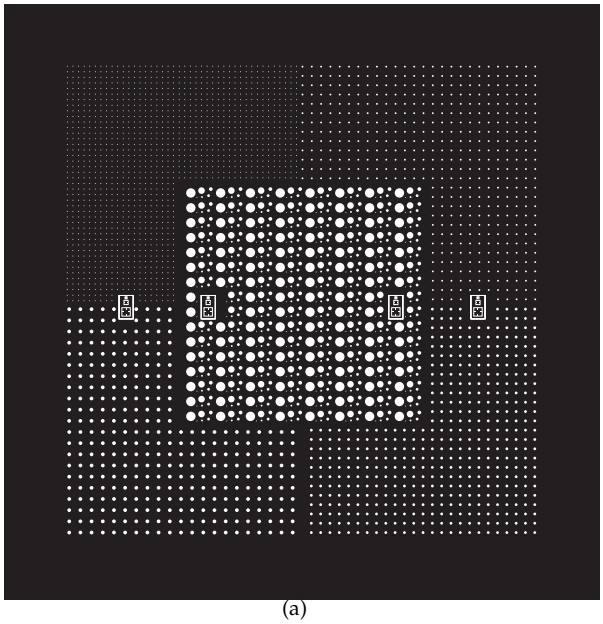

(a)

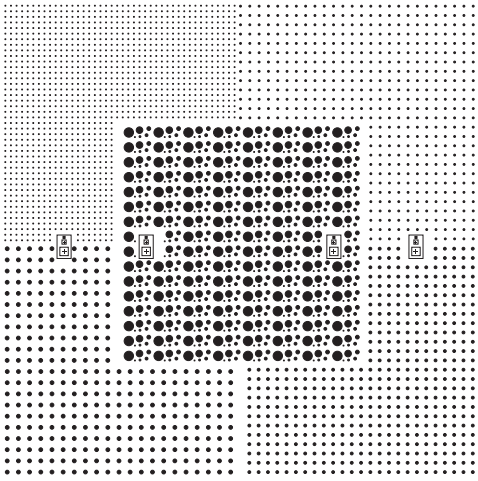

(b)

Figure A.2: Pattern of the 5″ masks used for patterning the a) oxide prior to eching holes for emitter formation and b) Al film prior to eching the Al islands for contacting the diodes.

remove the oxide layer that has been formed over the diodes during the diffusion process. To remove the backside oxide:

- Standard photoresist procedures are followed by spin coating the front side and hard baking at 120 °C for about 15 min.
- BOE etch to remove the backside oxide. Wait for hydrophobic behavior.
- Acetone to remove photoresist and Piranha etch to remove organics.
- RCA 1-3 to clean wafers before metalization.

Wafers are then loaded into a thermal evaporator for deposition of about 200 nm of Al. Positive photolitography with mask 2 (shown in Fig. A.2(b)) is then used to form islands of photoresist over the oxide holes. Primer should not be applied when working with Al films, as it will make development difficult. Further, it is important to get the alignment correct as shown in Fig.A.3. Exposure is done at 240 W for 8 s. The developer solution must be 1:6 of Dev:H_2O, or lower, as there is a risk of developing unexposed regions. In order to remove the exposed Al regions, a short etch in 16:1:1:2 of H_3PO_4:HNO_3:Acetic acid:H_2O heated to about 50 °C is applied. Finally, the wafers are rinsed in acetone and DI-water to remove the remaining photoresist. The structure should look as in Fig.A.1.

A.5 Final notes

This process works very well for low resistivity substrates, but for high resistivity *p*-type substrates the substrate-oxide interface provides a huge leakage current. It was found that removing the oxide while keeping the middle part of the Al-contact provided good diodes in these circumstances. The following procedure was applied:

- Spin coating the diodes with the primer
- Placing a droplet of photoresist on the Al-contact

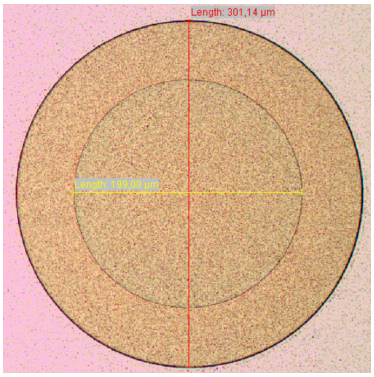

Figure A.3: Optical microscope image of the finished structure, showing good alignment.

- Hard baking at 125 °C for 15 min
- Al-etch to remove the edges over the oxide
- BOE etch to remove the oxide
- Rinse in acetone and Piranha etch

Bibliography

[1] URL http://lhc.web.cern.ch/lhc.

[2] URL http://rd50.web.cern.ch.

[3] C. Kittel. *Introduction to Solid State Physics*. John Wiley & sons, Inc, 8th edition, 2001.

[4] B.G. Streetman and S. Banerjee. *Solid State Electronic Devices*. Prentice Hall International, 6th edition, 2000.

[5] W. Shockley and W. T. Read. Statistics of the recombinations of holes and electrons. *Physical Review*, 87(5):835, 1952.

[6] R. N. Hall. Electron-hole recombination in germanium. *Physical Review*, 87(2):387, 1952.

[7] P. Blood and J.W. Orton. *The Electrical Characterization of Semiconductors: Majority Carriers and Electron States*, volume 14. Academic Press, 1991.

[8] O. Engström and A. Alm. Thermodynamical analysis of optimal recombination centers in thyristors. *Solid-State Electronics*, 21(11):1571–1576, 1978.

[9] J. A. Van Vechten and C. D. Thurmond. Entropy of ionization and temperature variation of ionization levels of defects in semiconductors. *Physical Review B*, 14(8):3539, 1976.

[10] D. V. Lang, J. D. Cohen, and J. P. Harbison. Measurement of the density of gap states in hydrogenated amorphous silicon by space charge spectroscopy. *Physical Review B*, 25:5285–5320, 1982.

[11] D.V. Lang. Deep-level transient spectroscopy: A new method to characterize traps in semiconductors. *Journal of Applied Physics*, 45, 1974.

[12] L. C. Kimerling and J. M. Poate. Lattice defects in semiconductors. *Institute of Physics Conference Series*, 23:126, 1974.

[13] L. C. Kimerling, H. M. DeAngelis, and J. W. Diebold. On the role of defect charge state in the stability of point defects in silicon. *Solid State Communications*, 16(1):171–174, 1975.

[14] L. C. Kimerling. New developments in defect studies in semiconductors. *IEEE Transactions on Nuclear Science*, 23:1497–1505, 1976.

[15] G. L. Miller, D. V. Lang, and L. C. Kimerling. Capacitance transient spectroscopy. *Annual Review of Materials Science*, 7(1):377–448, 1977.

[16] L. C. Kimerling, P. Blood, and W. M. Gibson. Defect states in proton-bombarded silicon at temperatures $\leq$ 300 K. *Defects and Radiation Effects in Semiconductors*, pages 273–280, 1978.

[17] A. A. Istratov. The resolution limit of traditional correlation functions for deep level transient spectroscopy. *Review of scientific instruments*, 68(10):3861–3865, 1997.

[18] A. A. Istratov. New correlation procedure for the improvement of resolution of deep level transient spectroscopy of semiconductors. *Journal of Applied Physics*, 82(6):2965, 1997.

[19] D Åberg. Capacitance spectroscopy of point defects in silicon and silicon carbide. PhD thesis, KTH, Royal Instutute of Technology, Stockholm, 2001 http://kth.diva-portal.org/smash/record.jsf?searchId=2&pid=diva2:8982.

[20] P. Pellegrino. Point defects in ion-implanted silicon and silicon carbide. PhD thesis, KTH, Royal Instutute of Technology, Stockholm, 2001 http://kth.diva-portal.org/smash/record.jsf?searchId=3&pid=diva2:8897.

[21] L. Dobaczewski, A. R. Peaker, and K. Bonde Nielsen. Laplace-transform deep-level spectroscopy: The technique and its applications to the study of point defects in semiconductors. *Journal of Applied Physics*, 96(9):4689–4728, 2004.

[22] URL http://www.laplacedlts.eu.

[23] P.E.J. Flewitt and R.K. Wild. *Physical methods for materials characterisation*. Institute of Physics Publishing, Bristol and Philadelphia, 2nd edition, 2003.

[24] L. Rubin and J. Poate. Ion implantation in silicon technology. *Industrial Physicist*, 9(3):12–15, 2003.

[25] W. Shockley. Forming semiconductive devices by ionic bombardment, April 2 1957. US Patent 2,787,564.

[26] B. G. Svensson, C. Jagadish, A. Hallén, and J. Lalita. Generation of vacancy-type point defects in single collision cascades during swift-ion bombardment of silicon. *Physical Review B*, 55(16):10498–10507, 1997.

[27] F. Auret and P. Deenapanray. Deep Level Transient Spectroscopy of Defects in High-Energy Light-Particle Irradiated Si. *Critical Reviews in Solid State & Materials Sciences*, 29:1–44, 2004.

[28] J. F. Ziegler, J. P. Biersack, and U. Littmark. The stopping and range of ions in matter. *Pergamon Press, New York*, 1985.

[29] D. M. Fleetwood, S. T. Pantelides, and R. D. Schrimpf. *Defects in Microelectronic Materials and Devices*. CRC, 2009.

[30] S. J. Pearton, J. W. Corbett, and T. S. Shi. Hydrogen in crystalline semiconductors. *Applied Physics A: Materials Science & Processing*, 43(3):153–195, 1987.

[31] E. V. Monakhov, A. Ulyashin, G. Alfieri, A. Yu. Kuznetsov, B. S. Avset, and B. G. Svensson. Divacancy annealing in si: Influence of hydrogen. *Physical Review B*, 69(15):153202, 2004.

[32] T. Zundel and J. Weber. Trap-limited hydrogen diffusion in boron-doped silicon. *Physical Review B*, 46(4):2071, 1992.

[33] J. W. Corbett and G. D. Watkins. Silicon divacancy and its direct production by electron irradiation. *Physical Review Letters*, 7(8):314–316, 1961.

[34] A. O. Evwaraye and E. Sun. Electron-irradiation-induced divacancy in lightly doped silicon. *Journal of Applied Physics*, 47(9):3776–3780, 1976.

[35] G. Bemski. Paramagnetic resonance in electron irradiated silicon. *Journal of Applied Physics*, 30(8):1195–1198, 1959.

[36] G. D. Watkins, J. W. Corbett, and R. M. Walker. Spin resonance in electron irradiated silicon. *Journal of Applied Physics*, 30(8):1198–1203, 1959.

[37] G. D. Watkins and J. W. Corbett. Defects in irradiated silicon: electron paramagnetic resonance and electron-nuclear double resonance of the si-e center. *Physical Review*, 134(5A):A1359, 1964.

[38] A. N. Larsen, A. Mesli, K. Bonde Nielsen, H. K. Nielsen, L. Dobaczewski, J. Adey, R. Jones, D. W. Palmer, P. R. Briddon, and S. Öberg. E center in silicon has a donor level in the band gap. *Physical Review Letters*, 97(10):106402, 2006.

[39] J. H. Bleka, E. V. Monakhov, B. S. Avset, and B. G. Svensson. Room-temperature annealing of vacancy-type defect in high-purity n-type si. *Physical Review B*, 76(23):233204, 2007.

[40] J. H. Bleka, L. Murin, E. V. Monakhov, B. S. Avset, and B. G. Svensson. On the identity of a crucial defect contributing to leakage current in silicon particle detectors. *Applied Physics Letters*, 92:132102, 2008.

[41] V. P Markevich, A. R Peaker, S. B Lastovskii, L. I Murin, J. Coutinho, V. J. B Torres, P. R Briddon, L. Dobaczewski, E. V Monakhov, and B. G Svensson. Trivacancy and trivacancy-oxygen complexes in silicon: Experiments and ab initio modeling. *Physical Review B*, 80(23):235207, 2009.

[42] A. R. Bean and R. C. Newman. Low temperature electron irradiation of silicon containing carbon. *Solid State Communications*, 8(3):175–177, 1970.

[43] G. D. Watkins and K. L. Brower. Epr observation of the isolated interstitial carbon atom in silicon. *Physical Review Letters*, 36(22):1329–1332, 1976.

[44] Y. H. Lee, L. J. Cheng, J. D. Gerson, P. M. Mooney, and J. W. Corbett. Carbon interstitial in electron-irradiated silicon. *Solid State Communications*, 21(1):109–111, 1977.

[45] L. W. Song and G. D. Watkins. Epr identification of the single-acceptor state of interstitial carbon in silicon. *Physical Review B*, 42(9):5759, 1990.

[46] LW Song, XD Zhan, BW Benson, and GD Watkins. Bistable interstitial-carbon–substitutional-carbon pair in silicon. *Physical Review B*, 42(9):5765–5783, 1990.

[47] MT Asom, JL Benton, R. Sauer, and LC Kimerling. Interstitial defect reactions in silicon. *Applied physics letters*, 51(4):256–258, 1987.

[48] P. M. Mooney, L. J. Cheng, M. Süli, J. D. Gerson, and J. W. Corbett. Defect energy levels in boron-doped silicon irradiated with 1-MeV electrons. *Physical Review B*, 15(8):3836–3843, 1977.

[49] L. Vines, E. V. Monakhov, A. Y. Kuznetsov, R. Kozłowski, P. Kaminski, and B. G. Svensson. Formation and origin of the dominating electron trap in irradiated p-type silicon. *Physical Review B*, 78(8):85205, 2008.

[50] K. Bonde Nielsen, L. Dobaczewski, K. Goscinski, R. Bendesen, O. Andersen, and B. Bech Nielsen. Deep levels of vacancy-hydrogen centers in silicon

studied by Laplace DLTS. *Physica B: Physics of Condensed Matter*, 273:167–170, 1999.

[51] Y. Tokuda and T. Seki. Interaction of hydrogen with the vacancy-oxygen pair produced in n-type silicon by electron irradiation. *Semiconductor science and technology*, 15:126, 2000.

[52] P. Lévêque, A. Hallén, B. G. Svensson, J. Wong-Leung, C. Jagadish, and V. Privitera. Identification of hydrogen related defects in proton implanted float-zone silicon. *The European physical journal. Applied physics*, 23:5–9, 2003.

[53] K. Irmscher, H. Klose, and K. Maass. Hydrogen-related deep levels in proton-bombarded silicon. *Journal of Physics C Solid State Physics*, 18(23):4591–4591, 1985.

[54] S. Fatima, C. Jagadish, J. Lalita, B. G. Svensson, and A. Hallen. Hydrogen interaction with implantation induced point defects in p-type silicon. *Journal of Applied Physics*, 85:2562, 1999.

[55] O. Feklisova, N. Yarykin, E. B. Yakimov, and J. Weber. Hydrogen interaction with defects in electron-irradiated silicon. *Physica B: Physics of Condensed Matter*, 273:235–238, 1999.

[56] O. Feklisova, N. Yarykin, E. B. Yakimov, and J. Weber. On the nature of hydrogen-related centers in p-type irradiated silicon. *Physica B: Condensed Matter*, 308:210–212, 2001.

[57] J. Coutinho, O. Andersen, L. Dobaczewski, K. Bonde Nielsen, A. R. Peaker, R. Jones, S. Öberg, and P. R. Briddon. Effect of stress on the energy levels of the vacancy-oxygen-hydrogen complex in si. *Physical Review B*, 68(18):184106, 2003.

[58] J. H. Bleka, I. Pintilie, E. V. Monakhov, B. S. Avset, and B. G. Svensson. Rapid annealing of the vacancy-oxygen center and the divacancy center by diffusing hydrogen in silicon. *Physical Review B*, 77(7):73206, 2008.

[59] S. K. Estreicher, A. Docaj, M. B. Bebek, D. J. Backlund, and M. Stavola. Hydrogen in c-rich si and the diffusion of vacancy–h complexes. *physica status solidi (a)*, 2012.

[60] R. Jones, B. J Coomer, J. P. Goss, B. Hourahine, and A. Resende. The interaction of hydrogen with deep level defects in silicon. *Solid State Phenomena*, 71:173–248, 1999.

[61] J. Coutinho, V. J. B. Torres, R. Jones, S. Öberg, and P. R. Briddon. Electronic structure of divacancy-hydrogen complexes in silicon. *Journal of Physics: Condensed Matter*, 15(39):S2809, 2003.

[62] K. Bothe and J. Schmidt. Electronically activated boron-oxygen-related recombination centers in crystalline silicon. *Journal of Applied Physics*, 99:013701, 2006.

[63] J. Schmidt and K. Bothe. Structure and transformation of the metastable boron-and oxygen-related defect center in crystalline silicon. *Physical Review B*, 69(2):024107, 2004.

[64] L. I. Murin, E. A. Tolkacheva, V. P. Markevich, A. R. Peaker, B. Hamilton, E. V. Monakhov, B. G. Svensson, J. L. Lindström, P. Santos, J. Coutinho, et al. The oxygen dimer in si: Its relationship to the light-induced degradation of si solar cells? *Applied Physics Letters*, 98:182101, 2011.

[65] D. Macdonald, F. Rougieux, A. Cuevas, B. Lim, J. Schmidt, M. Di Sabatino, and L. .J Geerligs. Light-induced boron-oxygen defect generation in compensated p-type czochralski silicon. *Journal of Applied Physics*, 105(9):093704–093704, 2009.

[66] V. V. Voronkov and R. Falster. Latent complexes of interstitial boron and oxygen dimers as a reason for degradation of silicon-based solar cells. *Journal of Applied Physics*, 107(5):053509–053509, 2010.

[67] A. Carvalho, P. Santos, J. Coutinho, R. Jones, M. J. Rayson, and P. R. Briddon. Light induced degradation in B doped Cz-si solar cells. *Physica Status Solidi (a)*, 2012.

[68] U. Gösele and T. Y Tan. Oxygen diffusion and thermal donor formation in silicon. *Applied Physics A: Materials Science & Processing*, 28(2):79–92, 1982.

[69] R. Balasundaraprabhu, E. V. Monakhov, N. Muthukumarasamy, O. Nilsen, and B. G. Svensson. Effect of heat treatment on ito film properties and ito/p-si interface. *Materials Chemistry and Physics*, 114(1):425–429, 2009.

[70] J. George and C. S. Menon. Electrical and optical properties of electron beam evaporated ITO thin films. *Surface and Coatings Technology*, 132(1):45 – 48, 2000.

[71] H. Kim, C. M. Gilmore, A. Piqué, J. S. Horwitz, H. Mattoussi, H. Murata, Z. H. Kafafi, and D. B. Chrisey. Electrical, optical, and structural properties of indium–tin–oxide thin films for organic light-emitting devices. *Journal of Applied Physics*, 86:6451, 1999.

[72] T. Maruyama and K. Fukui. Indium-tin oxide thin films prepared by chemical vapor deposition. *Journal of Applied Physics*, 70:3848–3851, 1991.

Paper I

Hydrogen-related defects in boron doped p-type silicon

H. Malmbekk, L. Vines, E.V. Monakhov, and B.G. Svensson,
*Phyica Status Solidi C **8**, No. 3, 705– 708 (2011); doi: 10.1002/pssc.201000260*

Paper II

Hydrogen decoration of vacancy related complexes in hydrogen implanted silicon

H. Malmbekk, L. Vines, E.V. Monakhov, and B.G. Svensson,
Solid State Phenomena Vols. 178-179 (2011) pp 192-19;
doi: 10.4028/www.scientific.net/SSP.178-179.192

Paper III

Comparative study of hydrogen-related defects in p- and n-type silicon

H. Malmbekk, L. Vines, B. G. Svensson, and E. V. Monakhov,
In Manuscript

Paper IV

Annealing dynamics of irradiation-induced defects in high-purity silicon in the presence of hydrogen

J. H. Bleka, H. Malmbekk, E. V. Monakhov, B. S. Avset, and B. G. Svensson,
*Physical Review B **85**, 085210 (2012); doi: 10.1103/PhysRevB.85.085210*

Annealing dynamics of irradiation-induced defects in high-purity silicon in the presence of hydrogen

J. H. Bleka,* H. Malmbekk,† E. V. Monakhov, and B. G. Svensson
Department of Physics, Physical Electronics, University of Oslo, P.O. Box 1048 Blindern, N-0316 Oslo, Norway

B. S. Avset
SINTEF ICT, Microsystems and Nanotechnology, P.O. Box 124 Blindern, N-0314 Oslo, Norway
(Received 8 December 2011; published 23 February 2012)

A reaction model explaining (i) the hydrogen-mediated transformation of the vacancy-oxygen (VO) center into a vacancy–oxygen-hydrogen center (VOH^*), with an energy level at 0.37 eV below the conduction-band edge (E_c), and (ii) the passivation of the divacancy center is presented. VOH^* dissociates with a rate of 2×10^{-5} s^{-1} at 195 °C, causing VO to recover after long duration ($>10^4$ min), while a similar evolution occurs at 300 °C on a time scale of the order of 10 min. The diffusivity of the monatomic hydrogen used in the model agrees closely with the established values for the diffusivity of protons. After the recovery of VO, further annealing at higher temperatures and/or longer durations transforms VO into the "ordinary" vacancy–oxygen-hydrogen center with an energy level at $E_c - 0.32$ eV (VOH). VOH is subsequently transformed into VOH_2. For temperatures above 250 °C, two additional hydrogen-related levels occur (~ 0.17 and ~ 0.58 eV below E_c) with a one-to-one ratio and a possible association with different charge states of a V_2OH center is discussed.

DOI: 10.1103/PhysRevB.85.085210 PACS number(s): 71.55.Cn, 66.30.J−, 61.80.Fe

I. INTRODUCTION

Hydrogen in Si readily reacts with vacancy-type defects by passivating the dangling bonds. It is known, for instance, that the vacancy-oxygen (VO) center and the divacancy (V_2) center disappear at temperatures below 300 °C in the presence of hydrogen.[1] The VO center transforms into a VOH center,[2–10] while the annealing mechanism for the V_2 center is less documented, although there have been several suggestions that the hydrogen-mediated annealing may give rise to a divacancy-hydrogen (V_2H) center.[2,9,11]

Reported values for the migration energy of monatomic hydrogen in Si range from 0.48 eV (Ref. 12) to 1.2 eV (Ref. 13) and, presumably, depend on the charge state of the hydrogen. This complicates the investigation of hydrogen-related defect reactions and calls for detailed isothermal annealing data in order to quantify the kinetics. In Ref. 11 it was shown that during annealing of H-diffused high-purity silicon at temperatures below 200 °C, monatomic hydrogen reacts with the vacancy-oxygen (VO) center to form what is considered to be an unstable vacancy–oxygen-hydrogen complex (VOH^*); this complex has an energy level at $E_c - 0.37$ eV (E_c being the energy of an electron at the conduction-band edge), in the following labeled as $E1$. At longer annealing times, VOH^* was seen to dissociate back to VO and monatomic hydrogen. The V_2 center was also observed to disappear due to monatomic hydrogen, but at a slightly higher rate than the VO center associated with a large capture radius. It was suggested that this results in a V_2H center. Thus, at these low annealing temperatures, the defect behavior can, in a first approximation, be described by the following reactions:

$$VO + H \rightarrow VOH^*, \quad (1)$$

$$VOH^* \rightarrow VO + H, \quad (2)$$

$$V_2 + H \rightarrow V_2H. \quad (3)$$

In the present contribution, we show that the result of a numerical simulation based on reactions (1)–(3) reproduces closely the experimental results in Ref. 11. Further, a second focus will be on the defect dynamics in H-diffused and H-implanted samples treated at higher temperatures and/or with longer durations than those used in Ref. 11 (>200 °C). In the latter case, VOH plays a central role while VOH^* is absent.

II. TECHNICAL DETAILS

Four different samples (A–D) were investigated. The samples A–C were p^+–n^-–n^+ Si diodes produced from high-purity detector-grade magnetic-Czochralski (MCz) and diffusion-oxygenated float zone (DOFZ) wafers with a phosphorus concentration of 5×10^{12} cm^{-3}. Hydrogen was introduced by submerging the samples in 10% hydrofluoric acid (HF) at 50 °C for $\frac{1}{2}$ h. Aluminium (Al) contacts were deposited on the MCz samples before irradiation at room temperature (RT) with 6-MeV electrons to a dose of 5×10^{12} cm^{-2}. The DOFZ samples were annealed for 1 h at 450 °C in nitrogen ambient prior to irradiation at RT with 15-MeV electrons to a dose of 2×10^{12} cm^{-2}. The contact material used for these samples was silver glue.

Sample D was a p^+–n Si diode prepared on a phosphorus-doped (1×10^{15} cm^{-3}) Cz wafer. Ohmic contacts to the p^+ layer were formed by thermal evaporation of Al and backside contacts were made by scratching silver glue onto the substrate. H-implantation was performed at an energy of 1110 keV through a 15 μm thick Al foil, yielding an average penetration depth of $\sim 2\,\mu$m in the Si substrate according to estimates by TRIM calculations.[14] The dose used was 8×10^{10} cm^{-2}, and the TRIM calculations suggest that the concentration of implanted H is at least one order of magnitude higher than the defect concentration anticipated to be detected by deep level transient spectroscopy (DLTS). This estimate accounts for that only a few percent of the generated vacancies survive dynamic annealing and form electrically active defects.[15]

The concentrations of oxygen and carbon in the different types of materials were measured by secondary-ion mass

TABLE I. Survey of the four samples investigated. Sample C was annealed between the hydrogenation and the irradiation.

Sample	Material	Oxygen conc.	Carbon conc.	Hydrogenation	Preirradiation annealing
A	MCz	$0.5–1 \times 10^{18}\,cm^{-3}$	$\leqslant 1 \times 10^{16}\,cm^{-3}$	HF	None
B	MCz	$0.5–1 \times 10^{18}\,cm^{-3}$	$\leqslant 1 \times 10^{16}\,cm^{-3}$	HF	None
C	DOFZ	$2–3 \times 10^{17}\,cm^{-3}$	$2–4 \times 10^{16}\,cm^{-3}$	HF	1 h at 450 °C
D	Cz	$\sim 10^{18}\,cm^{-3}$	$\sim 10^{16}\,cm^{-3}$	H-implant	None

spectrometry and are listed in Table I. The setups used for the DLTS measurements and depth-profiling measurements are based on a HP 4280A capacitance meter,[16] and a Boonton 7200 capacitance meter. Both a lock-in–type weighting function and a GS4 weighting function[17] were used to extract the DLTS signal. Subsequently, the concentration, energy-level position, and apparent capture cross section of the electron traps were derived.

III. ISOTHERMAL ANNEALING UP TO 225 °C

A. DLTS measurements

A H-diffused MCz sample (sample A in Table I) was isothermally annealed at 225 °C up to 16 320 min; Fig. 1 shows the DLTS spectra of this sample for the nonannealed state and after three different annealing times. After no annealing, the DLTS spectra show the well-known VO center, V_2 center, and interstitial-carbon–interstitial-oxygen (C_iO_i) center. After 20 min, the reactions (1) and (3) have caused a large growth in the concentration of VOH^* centers ($[VOH^*]$) and the disappearance of most of the V_2 centers, in accordance with that observed in Ref. 11. The energy level at about $E_v + 0.23$ eV, labeled $H1$, has also appeared with an amplitude similar to that of the loss of the V_2 peaks (E_v denotes the valence-band edge). As discussed in Ref. 11, this level may be due to the V_2H center resulting from reaction (3), although V_2H is, from *ab initio* calculations, expected also to have an energy level at about $E_c - 0.4$ eV, but no such level is detected in the H-diffused samples.[18] After 2560 min, the hydrogen has diffused deeper into the sample, and most of the VOH^* centers have dissociated through reaction (2). However, the VO peak is not fully recovered and is lower than the initial value. The V_2 center has disappeared completely, while $[H1]$ has been reduced only slightly. The "ordinary" vacancy–oxygen-hydrogen (VOH) center[2–10] ($E_c - 0.32$ eV) has started to emerge at this stage. From the forward-injection spectra in Fig. 1, a peak is also seen to evolve at around 125 K, labeled as $H2$. Although there still exists some controversy about this level, it has been assigned as a donor level of VOH by several authors.[10,19] The fact that the ($E_c - 0.32$ eV) and $H2$ levels show similar concentration and growth behavior supports this assignment. After 16 320 min, VOH^* is no longer visible, $[VO]$, $[H1]$ and $[C_iO_i]$ are all reduced by roughly a factor of 2, and $[VOH]$ has increased.

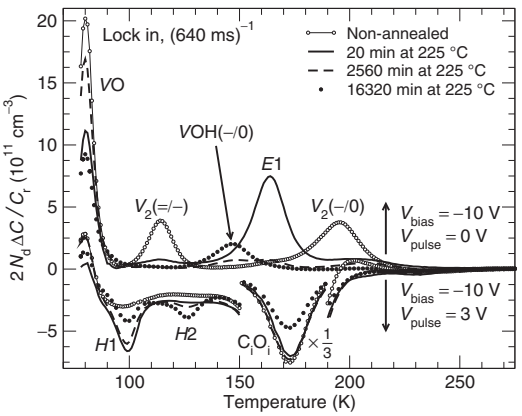

FIG. 1. DLTS spectra of sample A measured with ($V_{pulse} = 3$ V) and without ($V_{pulse} = 0$ V) forward injection after different annealing times at 225 °C. An estimate for the trap concentration, which does not account for the so-called lambda effect, can be read out at each of the peaks (Ref. 20). The nonannealed spectrum was not measured with forward injection and is therefore taken from sample B, which was prepared in parallel with sample A.

Figure 2 displays the trap concentration of a selection of the peaks observed in Fig. 1. Figure 2(a) shows in detail how $[VO]$ initially drops and is replaced by a similar amount of the VOH^* center before it reappears at the expense of the VOH^* center. The close relation between the variations in VO and VOH^* results in an almost constant (within ∼10%) sum of the two up to ∼1000 min (depicted as stars). For longer times, $[VO]$ is again reduced, but not replaced by the VOH^* center. This is, however, the stage where VOH emerges, although in a concentration smaller than the loss of $[VO]$. In Fig. 2(b), the sum of $[V_2]$ and $[H1]$ is seen to be rather constant initially, as discussed in great detail in Ref. 11. The uncertainty in $[H1]$ is substantial, but $[H1]$ decreases gradually at long annealing times.

For the H-implanted diode (sample D) (Fig. 3), the general picture is similar to that for the H-diffused samples discussed above. However, one major difference is that VOH occurs already after implantation without annealing, which is well known from the literature. In a similar manner to the H-diffused samples, $[E1]$ increases after 20 min at 225 °C, accompanied by an almost complete annealing of VO while $[VOH]$ remains constant. This confirms that VOH^* is the dominant complex forming during low-temperature annealing of VO in the presence of H. Further, relative to the in-diffused samples, sample D exhibits a major difference in the amplitude of the first and second acceptor levels of V_2. This has previously been attributed to that V_2H and the vacancy-phosphorus pair (VP) have very similar electron emission properties as the first acceptor level of V_2,[2,9,18] implying that V_2H forms directly during the implantation.

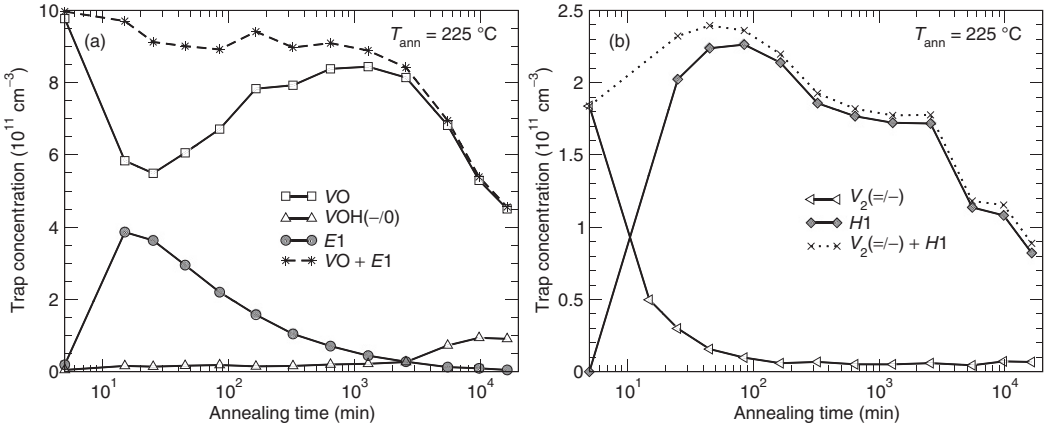

FIG. 2. Trap concentration versus annealing time deduced for the DLTS peaks arising from defects related to the VO center (a) and the V_2 center (b) (see Fig. 1). For the plot, an offset of 5 min was given to all the annealing times to allow for the initial amplitudes to be included on the logarithmic scale. [$H1$] was not measured after the 10-min anneal.

B. Depth distribution

1. Hydrogen-diffusion model at 195 °C

Figure 4 reveals how the depth profiles of [VO], [VOH^*], and [V_2] evolve during annealing at 195 °C for sample B. The sum of [VO] and [VOH^*] remains essentially constant as monatomic hydrogen diffuses in from the surface and temporarily transforms many of the VO centers into VOH^* centers. The defect behavior in Fig. 4 can be modeled rather well by the reactions (1), (2), and (3) together with in-diffusion of monatomic hydrogen from the surface. The solid lines in Fig. 4 are the result of this model, which yields the coupled differential equations in Table II, using the input parameters listed in Table III. The sample is treated as a uniform medium ranging from $x = -50\,\mu$m to $200\,\mu$m, and the surface is regarded as a reference plane at $x = 0$. The model assumes constant concentrations at the boundaries of the medium, but the extension of the medium is so large that the results are not affected if the boundary concentrations are set to zero, for instance, decreasing the initial concentrations linearly to zero from 20 μm away from the boundaries is found to have no influence when comparing with the experimental data. The simulation was run with the use of the function pdepe in MATLAB®. The input parameter values were optimized by an algorithm that changes the values and calculates the mean-square deviation from the measured depth profiles, keeping for the next iteration only those value sets that give a deviation smaller than the previously best.

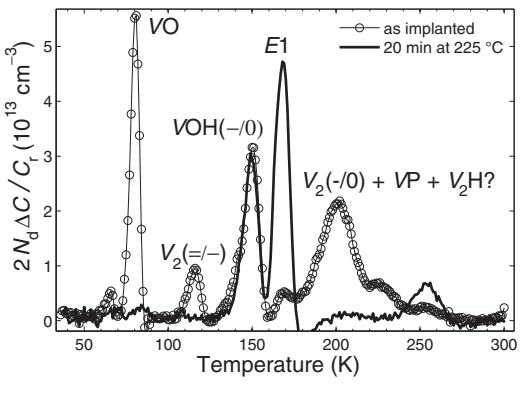

FIG. 3. DLTS spectra of the H-implanted sample D (8×10^{10} cm^{-2}) measured after implantation and after heat treatment at 225 °C. The spectra were deduced using the (640 ms)$^{-1}$ window of the GS4 weighting function (Ref. 17) to clearly resolve the $E1$ and VOH peaks.

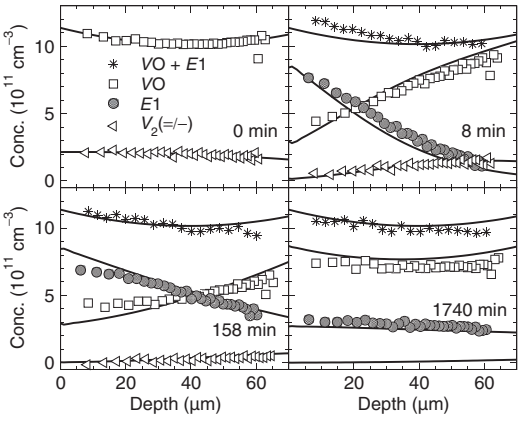

FIG. 4. Evolution of the depth profiles during annealing at 195 °C for sample B. The experimental data are from Ref. 11, and the solid lines are the result of the simulation described by Tables II and III. The profiles are corrected for the lambda effect.

TABLE II. Differential equations describing a model where only monatomic hydrogen is mobile and the immobile VO center captures hydrogen to form the VOH^* center. An unspecified center X, which traps hydrogen, is also included. All the concentrations are functions of the annealing time t and the depth x. The result of the simulation is shown in Fig. 4.

Defect species	Rate equation
H	$\frac{d[H]}{dt} = D_H \frac{d^2[H]}{dx^2} + \frac{d[VO]}{dt} - \frac{d[BH]}{dt} + \frac{d[V_2]}{dt} + \frac{d[X]}{dt}$
VO	$\frac{d[VO]}{dt} = -\frac{d[VOH^*]}{dt}$
VOH^*	$\frac{d[VOH^*]}{dt} = 4\pi R_{VO} D_H[H][VO] - C^{diss}_{VOH^*}[VOH^*]$
V_2	$\frac{d[V_2]}{dt} = -4\pi R_{V_2} D_H[H][V_2]$
BH	$\frac{d[BH]}{dt} = -C^{diss}_{BH}[BH]$
X	$\frac{d[X]}{dt} = -4\pi R_X D_H[H][X]$

A uniform concentration of hydrogen sinks ($[X]$) is also included in the model, but the result of the parameter optimization shows the optimum fit to the measured depth profiles when $[X] \approx 0$ (low concentration and/or small hydrogen-capture radius R_X). Hence, the influence by X is small and can be ignored. The modeling parameters listed in Table III are not fully unique in yielding such a close agreement with the experimental data as that displayed in Fig. 4. For instance, the 1-μm-deep surface concentration of the boron-hydrogen (BH) center, which is assumed to be the source of monatomic hydrogen, is known to have a dissociation barrier of 1.28 eV and a prefactor of 2.8×10^{14} s^{-1},[21] and is therefore mainly exhausted already after the initial 8-min anneal. Thus, the model is not particularly sensitive to the depth distribution of the initial concentration of hydrogen and the BH center. Furthermore, the hydrogen-capture radius of the VO center, R_{VO}, and that of V_2, R_{V_2}, can be reduced by several orders of magnitude if [BH] is increased by a corresponding factor. However, the value of 5×10^{-11} m used for R_{VO} seems to constitute an upper limit as larger capture radii cause steeper profiles and less correlation with the measured data. This value is still somewhat below 0.5 nm, normally used due to geometrical considerations, and suggests that reaction (1) may have an energy barrier. Although the value of R_{VO} can be varied by many orders of magnitude, R_{V_2} must always be a factor of 1.5–2 larger than R_{VO} to reproduce the measured $[V_2]$ data, presumably indicating a somewhat lower energy barrier for the reaction with V_2.

The dissociation rate of the VOH^* center, $C^{diss}_{VOH^*}$, can not be changed significantly without also affecting the result of the simulation. Dissociative processes normally have preexponential factors similar to the Debye frequency.[22] Typical values are in the range 10^{11}–10^{13} s^{-1}, which, with the value for $C^{diss}_{VOH^*}$ resulting from the model optimization, gives a dissociation energy in the range of 1.5–1.6 eV. One crucial result, corroborating the validity of the simulations, is that the optimal value (according to the method of least squares) of D_H, is only about a factor of 4 less than that obtained from the preexponential factor and migration barrier found by Van Wieringen and Warmoltz[12] using temperatures larger than 1000 °C. Weber *et al.*[23] later found that the values obtained by Wieringen and Warmoltz agree well with the diffusion properties of positively charged hydrogen atoms at RT.

2. *Extended annealing at 225 °C*

Figure 5 shows the depth profiles measured for sample A, treated at 225 °C. After 2560 min, the VOH^* center has, as demonstrated in Figs. 1 and 2, appeared and almost fully disappeared again. $[VOH]$ is not yet large enough to allow for a depth profile to be measured. $[VO]$ has, at this stage, first decreased significantly at the front surface side, then almost recovered to the initial concentration, and, subsequently, started to decrease again at the surface, similar to that seen in Fig. 4. After the 5500-min anneal, $[VO]$ has decreased mainly in the shallow region of the probing volume and $[VOH]$ is large enough to be profiled. Here, it should be noted that $[VOH]$ has a bell-shaped profile. After 9770 and 16 320 min, $[VO]$ is reduced further and $[VOH]$ is increased slightly, with the maximum gradually shifting to somewhat larger depths.

TABLE III. Parameters and values used for the equations in Table II. The diffusion coefficient, dissociation rates, and effective hydrogen-capture radii are specific to the modeling temperature of 195 °C.

Parameter	Explanation	Value	Comment
D_H	Diffusion coefficient of H	1.7×10^{-8} cm^2 s	Found by optimization
$C^{diss}_V OH^*$	Dissociation rate of VOH^*	2.3×10^{-5} s^{-1}	Found by optimization
C^{diss}_{BH}	Dissociation rate of BH	4.7 s^{-1}	Taken from Zundel and Weber (Ref. 21)
R_{VO}	Eff. H-capture radius of VO	5.0×10^{-11} m	Found to be the upper limit (see text)
R_{V_2}	Eff. H-capture radius of V_2	9.0×10^{-11} m	Found by optimization
R_X	Eff. H-capture radius of X	8.1×10^{-12} m	Found by optimization
$[H]_{t=0}$		0 cm^{-3}	Assumed zero
$[VO]_{t=0}$	Concentration at $t = 0$		Deduced from the experimental data and represented by a polynomial function
$[VOH^*]_{t=0}$		0 cm^{-3}	Assumed zero
$[V_2]_{t=0}$	Concentration at $t = 0$		Deduced from the experimental data and represented by a polynomial function
$[BH]_{t=0}$	Uniform conc. down to 1 μm	1.1×10^{14} cm^{-3}	Found by optimization
$[X]_{t=0}$	Uniform concentration	6.5×10^{10} cm^{-3}	Found by optimization (Note: $[X]_{t=0} \ll [VO]_{t=0}$)

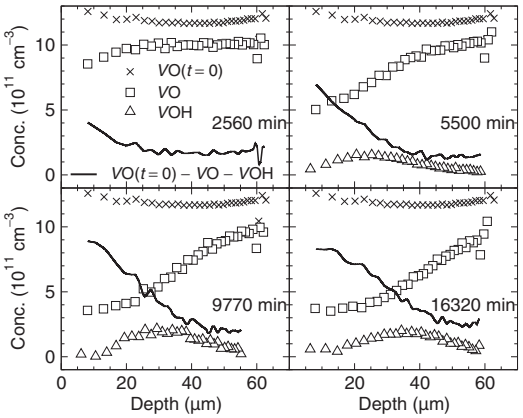

FIG. 5. Depth profiles of VO and VOH in sample A measured after long annealing times at 225 °C. The profiles are corrected for the lambda effect. The depth profiles were not measured in the nonannealed state and $VO(t = 0)$ is taken from the similar sample B.

The VOH center is expected to be generated by the reaction

$$VO + H \rightarrow VOH \tag{4}$$

as monatomic hydrogen diffuses in from the surface,[2–10] and VOH has a higher formation barrier than VOH^*.[11] As mentioned above, B-H as a hydrogen source is expected to be mainly exhausted already after an 8-min anneal at 195 °C. However, a flux of hydrogen is still present at 225 °C, as illustrated by the formation of VOH and presumably VOH_2. It also appears to be smaller as compared to that at 195 °C. Such a behavior of the hydrogen influx indicates the presence of at least one more hydrogen trap/reservoir at the near-surface region with higher thermal stability than that of B-H. Possible identification of the additional hydrogen trap/reservoir is speculative at this stage and may involve hydrogen-oxygen complexes and the interface between Si and the Al contact. The shape of the VOH profile can not be explained by reaction (4) alone if the hydrogen diffuses in from the surface. However, it can readily be accounted for by a sequence where reaction (4) is followed by an additional process where the VOH center is passivated by another (or the same) defect diffusing in from the surface:

$$VOH + Z \rightarrow VOHZ. \tag{5}$$

According to Pellegrino *et al.*,[8] Z is monatomic hydrogen and the result is the electrically inactive VOH_2 center.[10,24]

In H-poor samples, the VO center has been shown to anneal out via the reaction

$$VO + O_i \rightarrow VO_2, \tag{6}$$

where the diffusion coefficient of the VO center has an activation barrier of 2.06 eV and a prefactor of 22.9 cm^2 s.[25] At 225 °C, this gives a decrease in $[VO]$ of less than 10^{10} cm^{-3} in 10^4 s and will not contribute significantly to the observed loss. It appears, therefore, reasonable to assume that reaction (4) together with reaction (5) ($Z = H$) is the main route for the VO center to disappear in this temperature regime. Within this scenario, the initial $[VO]$ $[[VO](x,t = 0)]$ subtracted by $[VO](x,t)$ and $[VOH](x,t)$ yields $[VOH_2](x,t)$, assuming no further reactions of VOH_2. The result deduced is shown as the solid lines in Fig. 5, and indeed, the profiles obtained are plausible for a defect caused by in-diffusion of a reactant from the surface.

IV. ISOCHRONAL ANNEALING UP TO 400 °C

Figure 6 shows DLTS spectra of sample C annealed isochronally for 15 min from 175 °C to 400 °C in steps of 25 °C. Sample C was heat treated for 1 h at 450 °C after the HF and prior to the electron irradiation; in such pretreated samples, the generation of VOH^* still exists, but is strongly suppressed. This is attributed to the fact that the 450 °C treatment distributes hydrogen more homogeneously and the locally high hydrogen concentration promoting reaction (1) in samples without preannealing diminishes. The amplitude

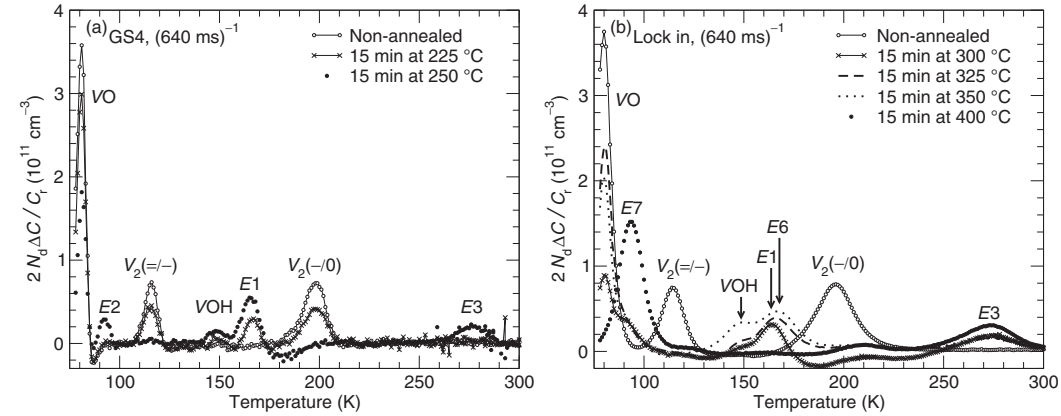

FIG. 6. DLTS spectra measured after isochronal annealing of the H-diffused DOFZ sample (sample C). The spectra in (a) are deduced using the 640-ms window of the GS4 weighting function (Ref. 17) to better separate the $E2$ peak from the VO peak.

of the $E1$ peak reaches its maximum value after the 250 °C anneal, where significant changes occur: $[VO]$ and $[V_2]$ decrease substantially, the VOH level emerges, and two new levels, labeled $E2$ and $E3$, appear, with energy positions of $E_c - 0.17$ eV and about $E_c - 0.58$ eV, respectively. These two levels seem to always appear simultaneously and with the same concentration. Hence, it is speculated that they are due to two different charge states of the same defect. We have only observed these levels in samples containing hydrogen and they occur with a higher concentration in oxygen-rich samples; hydrogen and oxygen may, thus, be part of the defect. V_2OH, formed by the reaction

$$V_2H + O_i \rightarrow V_2OH, \tag{7}$$

with V_2H as the mobile species is one possible assignment, although another level at $E_c - 0.44$ eV has previously been tentatively ascribed to V_2OH.[26]

As sample C is annealed sequentially for 15 min at 275 °C and 300 °C, no major changes take place except that $[VO]$ and $[VOH^*]$ decrease [Fig. 6(b)]. Even though VOH^* disappears after a few hundred minutes at 195 °C [Fig. 2(a)], it can remain after a 15-min anneal at 300 °C; typical values for $C_V^{\mathrm{diss}}OH^*$ (see Sec. III B 1) give up to a factor of ∼100 in difference between the annealing rates at 195 °C and 300 °C. At 325 °C, the VO peak grows strongly, while the $E1$ peak shifts to a higher temperature (peak labeled $E6$). Thus, VOH^* breaks up and causes an increase in $[VO]$, but $[VOH^*]$ is, by far, not sufficient to account for the large increase in $[VO]$. Since a substantial fraction of the initial VO centers is expected to be "stored" as VOH_2 (electrically inactive) at this stage, it may be suggested that VOH_2 breaks up and restores the VO center through the reactions

$$VOH_2 \rightarrow VOH + H, \tag{8}$$

$$VOH + H \rightarrow VO + 2H. \tag{9}$$

The existing data are not sufficient to determine whether VOH_2 breaks up directly ($VOH_2 \rightarrow VO + 2H$) or through the intermediate stage involving VOH, as indicated by reactions (8) and (9). Here, it should be emphasized that the signatures (energy position and capture cross section) of the growing peak at ∼80 K are identical with those of VO and we have no indications that the peak arises from a different defect than VO. During the subsequent annealing at 350 °C, $[VO]$ decreases slightly and $[VOH]$ increases correspondingly, possibly again due to reaction (4), but with a more stable source of monatomic hydrogen than when forming at 250 °C.

During the anneals at 375 °C and 400 °C, the VO, VOH, and $E6$ peaks disappear gradually, while $[E3]$ remains constant at 375 °C before increasing during the 400 °C anneal. Most noteworthy in this regime is the strong growth of the $E7$ peak, which is different from the $E2$ peak, as the position of the latter is 2 K lower. The identity of the $E7$ level is not known, although it is, as $E2$ and $E3$, only observed in H-diffused samples with a large oxygen concentration.

V. CONCLUSION

A defect reaction model where monatomic hydrogen diffuses in from the sample surface and (i) temporarily bonds with VO to form VOH^* and (ii) strongly bonds with V_2 to form V_2H was shown to reproduce closely the experimental concentration-versus-depth profiles of VO, VOH^*, and V_2 during long annealing at 195 °C. In particular, the VO center is first transformed into VOH^*, which later breaks up and VO reappears. We have confirmed formation of VOH^* in both lightly (5×10^{12} cm^{-3}) and moderately (1×10^{15} cm^{-3}) doped n-type samples. The extracted hydrogen diffusivity agrees well with that reported in the literature for H^+. In samples with a homogeneous distribution of hydrogen prior to irradiation, VOH^* persist after short anneals (15 min) up to ⩾300 °C before VO recovers and VOH starts to grow significantly. In these samples, also two additional hydrogen-related levels emerge at ∼250 °C, tentatively ascribed to different charge states of the V_2OH center.

For extended annealing at 225 °C (several days) and short annealing (⩽15 min) above 300 °C, monatomic hydrogen reacts with the VO center, resulting in the VOH center, which is more stable than the VOH^* center. The higher temperature required for the formation of VOH compared to that of VOH^* is taken as a clear evidence that the formation of VOH has a reaction barrier. Further, the VOH center disappears due to yet another release of monatomic hydrogen from the surface that causes the electrically inactive VOH_2 center to form. In contrast to VO, V_2 does not reappear after long annealing durations at 195 °C and its loss exhibits a one-to-one proportionality with the growth of $H1$ ($E_v + 0.23$ eV), corroborating an assignment of $H1$ to V_2H as discussed previously in the literature.

ACKNOWLEDGMENT

Financial support by the Norwegian Research Council is greatly appreciated.

*janhb@fys.uio.no
†helge.malmbekk@smn.uio.no

[1] E. V. Monakhov, A. Ulyashin, G. Alfieri, A. Y. Kuznetsov, B. S. Avset, and B. G. Svensson, Phys. Rev. B **69**, 153202 (2004).
[2] K. Bonde Nielsen, L. Dobaczewski, K. Goscinski, R. Bendesen, O. Andersen, and B. Bech Nielsen, Phys. B (Amsterdam) **273-274**, 167 (1999).
[3] B. G. Svensson, A. Hallén, and B. U. R. Sundqvist, Mater. Sci. Eng. B **4**, 285 (1989).
[4] K. Irmscher, H. Klose, and K. Maass, J. Phys. C: Solid State Phys. **17**, 6317 (1984).
[5] A. R. Peaker, J. H. Evans-Freeman, P. Y. Y. Kan, L. Rubaldo, I. D. Hawkins, K. D. Vernon-Parry, and L. Dobaczewski, Phys. B (Amsterdam) **273-274**, 243 (1999).
[6] Y. Tokuda and T. Seki, Semicond. Sci. Technol. **15**, 126 (2000).

[7]P. Lévêque, P. Pellegrino, A. Hallén, B. G. Svensson, and V. Privitera, Nucl. Instrum. Methods Phys. Res., Sect. B **174**, 297 (2001).
[8]P. Pellegrino, P. Lévêque, J. Lalita, A. Hallén, C. Jagadish, and B. G. Svensson, Phys. Rev. B **64**, 195211 (2001).
[9]P. Lévêque, A. Hallén, B. G. Svensson, J. Wong-Leung, C. Jagadish, and V. Privitera, Eur. Phys. J. Appl. Phys. **23**, 5 (2003).
[10]J. Coutinho, O. Andersen, L. Dobaczewski, K. B. Nielsen, A. R. Peaker, R. Jones, S. Öberg, and P. R. Briddon, Phys. Rev. B **68**, 184106 (2003).
[11]J. H. Bleka, I. Pintilie, E. V. Monakhov, B. S. Avset, and B. G. Svensson, Phys. Rev. B **77**, 073206 (2008).
[12]A. Van Wieringen and N. Warmoltz, Phys. (Amsterdam) **22**, 849 (1956).
[13]R. C. Newman, J. H. Tucker, A. R. Brown, and S. A. McQuaid, J. Appl. Phys. **70**, 3061 (1991).
[14]J. F. Ziegler, J. P. Biersack, and U. Littmark, *The Stopping and Range of Ions in Matter* (Pergamon, New York, 1985).
[15]B. G. Svensson, C. Jagadish, A. Hallen, and J. Lalita, Phys. Rev. B **55**, 10498 (1997).
[16]B. G. Svensson, K.-H. Rydén, and B. M. S. Lewerentz, J. Appl. Phys. **66**, 1699 (1989).
[17]A. A. Istratov, J. Appl. Phys. **82**, 2965 (1997).
[18]J. Coutinho, V. J. B. Torres, R. Jones, S. Öberg, and P. R. Briddon, J. Phys.: Condens. Matter **15**, S2809 (2003).
[19]O. Feklisova, N. Yarykin, E. Yakimov, and J. Weber, Phys. B: Condensed Matter **308**, 210 (2001).
[20]D. V. Lang, J. Appl. Phys. **45**, 3023 (1974).
[21]T. Zundel and J. Weber, Phys. Rev. B **39**, 13549 (1989).
[22]J. W. Corbett, *Electron Radiation Damage in Semiconductors and Metals* (Academic, New York, 1966), p. 39.
[23]J. Weber, S. Knack, O. V. Feklisova, N. A. Yarykin, and E. B. Yakimov, Microelectron. Eng. **66**, 320 (2003).
[24]V. P. Markevich, L. I. Murin, M. Suezawa, J. L. Lindström, J. Coutinho, R. Jones, P. R. Briddon, and S. Öberg, Phys. Rev. B **61**, 12964 (2000).
[25]M. Mikelsen, J. H. Bleka, J. S. Christensen, E. V. Monakhov, B. G. Svensson, J. Härkönen, and B. S. Avset, Phys. Rev. B **75**, 155202 (2007).
[26]M. Mikelsen, E. V. Monakhov, G. Alfieri, B. S. Avset, J. Härkönen, and B. G. Svensson, J. Phys.: Condens. Matter **17**, S2247 (2005).

Paper V

Electronic states at the interface between indium tin oxide and silicon

H. Malmbekk, L. Vines, E.V. Monakhov, and B.G. Svensson,
Journal of Applied Physics ***110****, 074503 (2011); doi: 10.1063/1.3643002*

Electronic states at the interface between indium tin oxide and silicon

H. Malmbekk,[a] L. Vines, E. V. Monakhov, and B. G. Svensson
University of Oslo, Physics Department/Center for Materials Science and Nanotechnology, P.O. Box 1048, Blindern, Oslo N-0316, Norway

(Received 28 March 2011; accepted 24 August 2011; published online 3 October 2011)

Electronic properties and thermal stability of interfacial states between indium tin oxide (ITO) and monocrystalline silicon (Si) have been investigated. ITO films with thicknesses of about 300 nm were deposited by dc magnetron sputtering on *n*- and *p*-type (100) Si at room temperature. The samples were then annealed for 30 min at different temperatures in the range 100–600 °C, and the ITO-Si junction was found to exhibit rectifying behavior. Current-voltage (IV), capacitance-voltage (CV), and deep-level transient spectroscopy (DLTS) measurements have been used to electrically characterize the ITO-Si interface. DLTS measurements on *p*-type Si samples reveal a dominant hole trap at around 0.37 eV above the valence band edge. In the *n*-type samples, a broad band of electron traps occur in the range 0.1-0.2 eV below the conduction band edge. These electron traps display wide DLTS peaks, indicating a band of electronic energy levels rather than well-defined states originating from isolated point defects. All the traps in both the *p*- and *n*-type samples are found to be located near the ITO-Si interface. Investigations of the thermal stability of the observed electronic states show that the dominant hole trap anneal out after 30 min at 250 °C, while the dominant electron traps can be stable up to 500 °C. IV and DLTS measurements demonstrate a clear correlation between the annealing of the dominant electronic states and increase in the junction rectification. © *2011 American Institute of Physics*. [doi:10.1063/1.3643002]

I. INTRODUCTION

Transparent conducting oxides (TCO) can form rectifying contacts to silicon, enabling fabrication of so-called Schottky solar cells.[1] Tin-doped indium oxide (ITO) is the most widely used TCO today, and ITO/Si heterostructures have some advantages over standard diffused emitter cells, a better short wavelength response, and a low thermal budget during fabrication. However, despite an improved blue-light response, the Schottky ITO/Si cells have so far reached efficiencies of only about 13%,[2] and one of the limiting factors is the quality of the ITO/Si interface. It has been reported, for instance, that an insulating oxide between ITO and Si, which influences the properties of the heterostructure, can occur.[3,4] Charges in the oxide, as well as defects at its interface with ITO and Si, can severely reduce the device performance,[5] and hence, a better understanding of the limiting processes must be established before these structures can reach their full potential.

Another solar cell design utilizing TCO films is the heterojunction with intrinsic thin layer (HIT) cell structure, where a hydrogen rich amorphous Si layer (a-Si:H) is used as the emitter, while the TCO acts as a front contact.[6–8] Hydrogen passivates defects in the a-Si emitter, and the a-Si:H layer provides good interface passivation to the Si wafer.[9] A structure based on this concept was recently demonstrated to exhibit an efficiency above 22%.[10] However, the nature of the current flow across the HIT structure is not fully understood, and in particular, the interfaces between the different layers are challenging to optimize. In order to improve the understanding of the TCO/a-Si:H interface, electrical techniques, such as deep-level transient spectroscopy (DLTS), can give information about recombination centers at the interface. Hence, studies of the ITO/Si interface are relevant both for HIT and Schottky cells, even though the structures are different.

Only a few DLTS studies of ITO/Si junctions have been published in the literature. Zettler *et al.*[11] investigated samples of ITO films sputtered on (111) *n*- and *p*-Si using a gas mixture of Ar and O_2. The samples were subsequently annealed in either N_2 or H_2 atmosphere, and the following conclusions were reached: i) multiple hole and electron traps are present, related to radiation damage, hydrogen, and/or ITO elements; ii) for both the ITO/*n*-Si and ITO/*p*-Si junctions, an annealing temperature of 400 °C is insufficient to remove all the traps; and iii) trap levels occur at large depths into the Si substrate, and they are attributed to channeling effects during the sputter deposition.

Kuwano and Ashok[12] conducted a similar study employing samples of sputtered ITO films on (100) Si and investigated the effects of hydrogen passivation and low temperature (<200 °C) annealing on the interface defects. They detected three electron traps at 0.10, 0.19, and 0.25 eV below the conduction band edge (E_c) and one hole trap at 0.20 eV above the valence band edge (E_v), where the traps at $E_c - 0.19$ eV and $E_c - 0.25$ eV decreased by up to 50% after annealing at 180 °C (12 h). Pre-hydrogenation of the Si wafers was shown to reduce the overall trap concentration by about 50%, and only one broad DLTS peak was obtained for both *p* and *n*-type substrates.

Recently, Monakhov *et al.*[13] reported on the presence of a hole trap $E_v + 0.3$ eV at the interface between sputtered

[a]Electronic mail: helge.malmbekk@smn.uio.no.

ITO films and (100) *p*-Si wafers. Post-deposition heat treatment at 300 °C (30 min in air) was found to be sufficient for annealing of the trap, and concurrently, improvements in both current-voltage (IV) and capacitance-voltage (CV) characteristics occurred.

In this work, the interface between sputter-deposited ITO films and both *n*- and *p*-type Si substrates have been investigated by transient spectroscopy techniques, and the results are correlated with chemical concentration versus depth profiles obtained by secondary ion mass spectrometry (SIMS). Further, post-deposition treatments for all investigated samples have been extended up to 600 °C, as compared to previous works. Hole traps are found to anneal out at ~250 °C, while electron traps persist even at 500 °C. In contrast to the previous works,[11,12] where complete annealing of the dominant electron trap was not observed, we obtain an almost complete loss of these traps at a temperature above ~500 °C. The traps exhibit a strong impact on the rectifying properties of the ITO/Si junction, and their origin is discussed based on the correlation with SIMS data.

II. EXPERIMENTAL DETAILS

The samples used consist of ITO films sputtered from a 99.98% In_2O_3:SnO_2(9:1) target (8 inches in diameter), onto cleaned and HF-etched (100) *p*- and *n*-type Cz-Si wafers (~ 500 μm thickness with a resistivity of 7–13 and 3–9 Ωcm, respectively) using a dc magnetron sputtering system (CVC type AST-601). The sample chamber was evacuated to a base pressure of 3 μTorr before an argon pressure of 2.5 mTorr was established, and deposition was undertaken at room temperature. During the 10 min deposition, a constant power density of 2.7 W/cm^2, as well as a rotation of the sample holder of 6 rpm, was maintained. These deposition parameters were chosen based on results from earlier works in order to prepare films with optimized electrical, optical, and structural properties.[14] The thickness of the ITO films was ~ 300 nm, as measured by both ellipsometery (AutoEL® Rudolph) and surface stylus profilometry (Veeco Dektak® 8 stylus profiler).

Samples were then subjected to a lithography process in order to form individual diodes on the substrates, in which a hard baking step was performed for up to 30 min at 120 °C on a hotplate, and therefore, none of the diodes can be regarded as truly "as-deposited". Subsequently, heat treatments were performed for 30 min in the temperature range 100–600 °C in a controlled cleanroom atmosphere with about 20% relative humidity. Four-point probe measurements were conducted to deduce the resistivity of the heat treated films (not subjected to the lithography process) and current-voltage (IV) measurements were undertaken to study the rectifying properties of the junctions using a Keithley 617 electrometer. Capacitance-voltage (CV) measurements were performed to determine carrier concentration versus depth profiles, and they were carried out at room temperature with a probe frequency of 1 MHz using an HP4280 A capacitance meter.

The DLTS measurements were performed in the temperature range 77-300 K with a setup described elsewhere.[15] The DLTS signal was averaged over 1 K and extracted by a lock-in weighting function, and up to eight different spectra were obtained from rate windows in the range (20 ms)$^{-1}$ to (2560 ms)$^{-1}$.

Chemical analysis was carried out using a Cameca IMS 7 F magnetic sector instrument, yielding depth profiles of impurity and matrix elements for deposited and annealed samples which were not subjected to the lithography process described above. A 10 keV O_2^+ primary beam with a current of 20 nA was rastered over an area of 200 × 200 μm^2, and positive secondary ions emitted from the central part (62 μm in diameter) of the sputtered crater were recorded. A constant erosion rate was assumed for depth calibration, and the crater depths were measured using a Veeco Dektak® 8 stylus profiler.

III. RESULTS AND DISCUSSION

A. SIMS measurements

Mass spectra were recorded in order to identify the most abundant elements, and on the basis of these results, depth profiles of hydrogen (H), carbon (C), oxygen (O), silicon (Si), indium (In), and tin (Sn) have been obtained after all the annealing treatments. Figure 1 shows the secondary ion intensities in counts/s versus depth for an as-deposited ITO/*p*-Si sample. Some trends are revealed:

(i) An interface transition region of about 50 nm in thickness is observed by SIMS after all the anneals, and the In and Si signals remain similar in all the samples. The extension of the interface region is much larger than the thickness of the native SiO_2 layer (~1 nm) expected to be present on the Si surface prior to the ITO deposition, and it is partly limited by the surface roughness of the films (~3 nm), as determined by atomic force microscopy (AFM) as well as by sputter-induced surface roughening, which is estimated to be also in the range of 3 nm.

(ii) The H and C signals exhibit a distinct peak within the interface region, where the H signal decreases for higher annealing temperatures (see Fig. 2(a)), while the C signal appears to be stable. Possible in-diffusion of H from the air during annealing is regarded as negligible compared to the

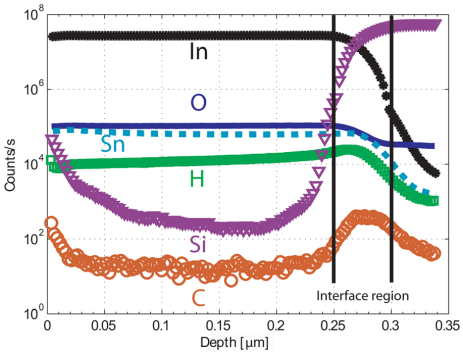

FIG. 1. (Color online) Depth profiles of as-deposited ITO/*p*-Si sample obtained by SIMS.

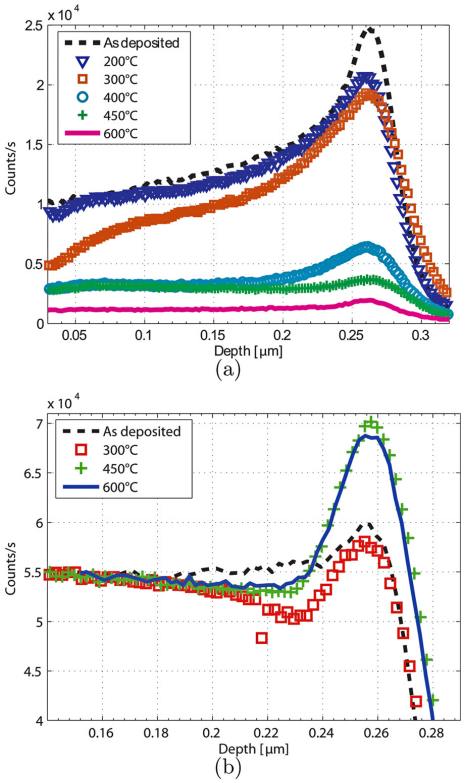

FIG. 2. (Color online) Depth profiles of (a) H and (b) Sn in ITO/*p*-Si sample obtained by SIMS (the profiles for Sn have been normalized to a joint bulk level).

level of H incorporated within the film, as the SIMS profiles show a reduction in the H concentration with increasing annealing temperature.

(iii) In contrast to that for In and Si, the signal of Sn displays an evolution as a function of annealing temperature (see Fig. 2(b)). The Sn signal becomes more confined to the interface region with increasing temperature, and this holds especially for the 450–600 °C range. Here, it should be emphasized that matrix effects may strongly affect the ionization efficiency of Sn atoms when profiling the interface region, and quantitative conclusions cannot be made. However, the evolution of the Sn signal shows unambiguously that changes take place at the ITO/Si interface with annealing, possibly affecting the abruptness and composition.

The Si and C signals in the film are relatively low, with a possible exception in the near surface region, and primarily attributed to C and Si impurities incorporated unintentionally during the sputtering process. The O-signal in Fig. 1 arises both from the ITO-film and the oxygen atoms incorporated by the sputtering O_2-beam, and it shows a uniform distribution throughout the film before reaching the interface region.

B. ITO properties

Figure 3 depicts the surface resistivity as a function of post-deposition annealing temperature for the ITO films (results are also included for control samples with fused silica (SiO_2) as substrate). A *low resistivity n-type region* occurs for the annealing temperatures 250-400 °C, with surface resistivity values in the range of $(3\text{-}4) \times 10^{-4}$ Ωcm. Table I compares the minimum values obtained in this study with those reported by other authors.[14,16–19] For a variety of different deposition techniques, with or without substrate heating, the ITO films possess resistivities in the 10^{-4} Ωcm range after exposure to temperatures of 250 to 400 °C.

C. Schottky contact characterization

From CV measurements, a net carrier concentration of 9.3×10^{14} and 1.5×10^{15} cm^{-3} for the *n*- and *p*-doped Si substrates, respectively, was deduced. For the ITO/*p*-Si samples at low reverse bias, the $1/C^2$ curves deviate from linearity for annealing at 120 °C (see Fig. 4). A similar behavior was also reported by Balasundaraprabhu *et al.*[14] for as-deposited and 100 °C annealed ITO/*p*-Si samples. As the slope of the $1/C^2$ curve is proportional to the inverse of the net carrier concentration, the large slope at low biases may be related to a considerable amount of interface defects of donor type, as proposed in Ref. 14, and/or passivation of the boron acceptors in the near Si-surface region. Accordingly, the ITO/*n*-Si samples do not show a deviation from linearity for any of the annealing temperatures, but the built-in voltage is found to vary in the 0.1-0.8 V range, increasing with annealing temperature (Fig. 4). A built-in voltage of 0.44 V was deduced for the ITO/*p*-Si samples, which is about 0.1 V higher than previously reported values.[14]

The current voltage data depicted in Fig. 5 reveal that the ITO/*n*-Si samples exhibit rectification for all the annealing temperatures, but a substantial improvement occurs above 450 °C, consistent with the increase in the built-in voltage. The ITO/*p*-Si samples generally show poorer rectification than the *n*-type ones; the highest rectification is obtained after the 250 and 300 °C anneals, while annealing above 400-450 °C results in

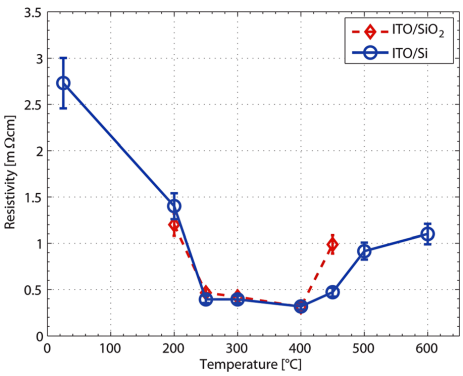

FIG. 3. (Color online) Surface resistivity of ITO films after different annealing temperatures.

TABLE I. Comparison of minimum resistivity values obtained for the ITO films in this work with those reported in Refs. 14 and 16–19.

Resistivity (Ωcm)	Annealing temperature	Substrate temperature	Report
3×10^{-4}	400 °C, 30 min	RT	Current
2.5×10^{-4}	300 °C, 30 min	RT	Ref. 14
3×10^{-4}	–	350 °C	Ref. 16
2×10^{-4}	–	300 °C	Ref. 17
$(1.6\text{-}1.8) \times 10^{-4}$	400 °C, 30-45 min	RT	Ref. 18
8.6×10^{-5}	–	250 °C	Ref. 19

Ohmic behavior, consistent with the results of Balasundaraprabhu *et al.*[14] and Chebotareva *et al.*[20]

D. Interface states

To investigate the presence of interfacial defects at the ITO/Si junction and to distinguish from bulk defects, the DLTS measurements were conducted with and without a forward biasing during the filling pulse. In the latter case, the interface is not probed, but the bulk only, and no DLTS signal is recorded above the detection limit. However, in the former case, a substantial signal is detected, in accordance with the results in Ref. 13, which provides strong evidence

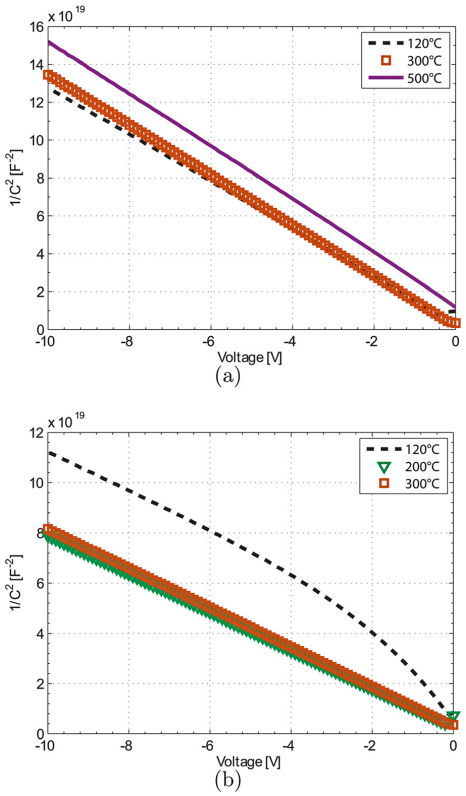

FIG. 4. (Color online) $1/C^2$ plot for the (a) ITO/*n*-Si samples and (b) ITO/*p*-Si samples. Reverse bias has been defined as negative voltage for both ITO/*n*-Si and ITO/*p*-Si samples.

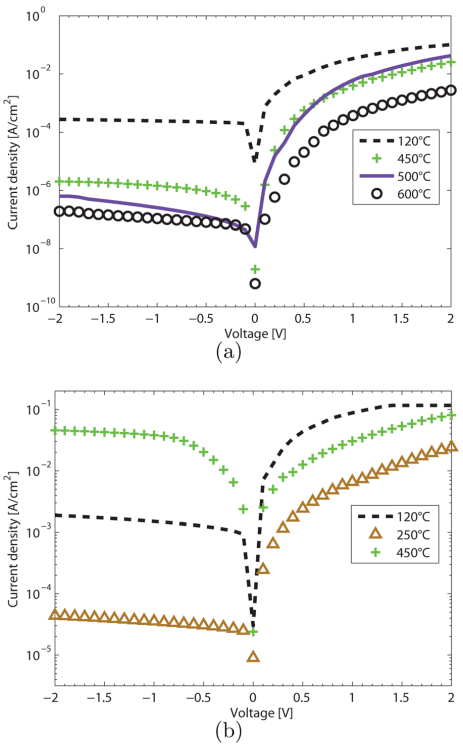

FIG. 5. (Color online) Current-voltage plot for (a) ITO/*n*-Si samples and (b) ITO/*p*-Si samples. Reverse bias has been defined as negative voltage for both ITO/*n*-Si and ITO/*p*-Si samples.

that the observed defects are located at or close to the ITO/Si interface. Figure 6(a) shows DLTS spectra of the ITO/*n*-Si samples and a multitude of electron traps in the energy range ~0.1–0.2 eV below E_c are revealed. The dominant level seen after the annealing step at 250 °C has been labeled as E(0.2) (as opposed to E(0.1) for all the other annealing steps), as it is deeper than all the other E(0.1) levels seen in Fig. 6(a). In addition, after the 120 °C anneal, a minor level occurs at $\sim E_c - 0.5$ eV (labeled as E(0.5) in Fig. 6(a)), but it disappears after 200 °C. The trap properties are summarized in Table II.

After the 450 °C annealing of the ITO/*n*-Si samples, no electron traps were detected, but only a weak indication of a hole trap. However, after annealing above 450 °C, the built-in voltage of the junction increases to about 0.8 V, implying that a forward bias of 0.5 V (used for filling in the measurements shown in Fig. 6(a)), is insufficient to fill electron traps located close to the ITO/Si interface. Indeed, using a forward bias of 2 V for filling (as seen in Fig. 6(b)), the major electron traps at $E_c - 0.1$ eV are still present after the 450 °C anneal. However, they are reduced by about 80% in strength after the 500 °C anneal, and after treatment at 600 °C, only a level at $\sim E_c - 0.4$ eV appears (labeled as E(0.4)). The concentration of E(0.4) is less than 20% of the dominant levels observed up to 450 °C. Measurements with a forward filling-

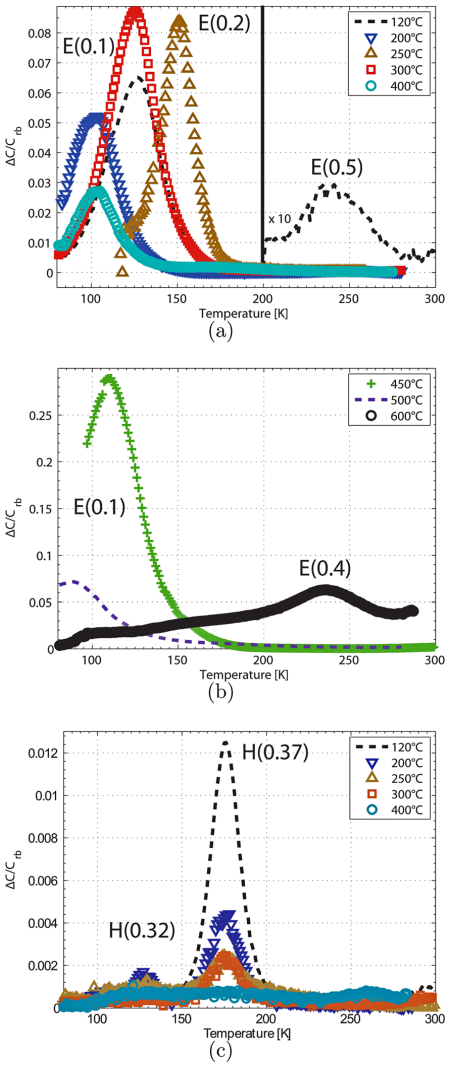

FIG. 6. (Color online) DLTS spectra of (a) ITO/*n*-Si. $V_r = -1$ V, $V_p = 0.5$ V. (b) ITO/*n*-Si. $V_r = -1$ V, $V_p = 2$ V. (c) ITO/*p*-Si samples. $V_r = -1$ V, $V_p = 0.5$ V. Rate window for all spectra in (a)-(c) is (640 ms)$^{-1}$. Reverse bias has been defined as negative voltage for both ITO/*n*-Si and ITO/*p*-Si samples.

pulse-voltage of 2 V were carried out for the lower annealing temperatures as well and showed comparable peak heights as for the 450 °C anneal in Fig. 6(b). From the measured concentration of interface traps extracted from Fig. 6, the sheet density of interface traps is estimated in the range of (10^{10}–10^{12}) cm^{-2} for the ITO/*n*-Si samples and about one order of magnitude lower for the ITO/*p*-Si samples. Here, it should be pointed out that the so-called λ-effect has not been taken into account and our focus is on the qualitative differences between the different anneals rather than on the absolute measure of the defect concentrations at the interface.

TABLE II. Trap properties.

Trap label	Energy level (eV)	$\sigma_{n(p)a}$ (cm^2)	Anneals
H(0.37)	$E_v + 0.37$	10^{-15}	250 °C
H(0.32)	$E_v + 0.32$	10^{-13}	250 °C
E(0.1)	$(E_c - 0.05) - (E_c - 0.15)$	$10^{-19} - 10^{-22}$	500 °C
E(0.2)	$(E_c - 0.14) - (E_c - 0.25)$	$10^{-16} - 10^{-19}$	500 °C
E(0.4)	$E_c - 0.4$	10^{-18}	> 600 °C
E(0.5)	$E_c - 0.5$	10^{-16}	200 °C

Figure 6(c) shows the DLTS spectra of the ITO/*p*-Si samples. One major hole trap appears at $E_v + 0.37$ eV (labeled as H(0.37)), and a smaller one appears at $E_v + 0.32$ eV (labeled as H(0.32)). H(0.37) decreases substantially in strength at 200 °C and even further at 250 °C and is below the detection limit after the 400 °C treatment. The H(0.32) level is less stable than H(0.37) and anneals out at 250 °C.

Figure 7 shows the Arrhenius plots for the H(0.37), E(0.1), and E(0.2) peaks. The two latter ones have quite broad DLTS peaks (Figs. 6(a) and 6(b)) suggesting several overlapping levels or a band of levels, and their corresponding Arrhenius plots are non-linear, providing additional evidence for the contribution from a manifold of levels. In contrast, the H(0.37) peak is narrow, with a width close to that expected theoretically for an isolated point defect, and it exhibits a linear Arrhenius behavior. The non-linearity of E(0.1) and E(0.2) occurs for all the spectra in Figs. 6(a) and 6(b), with minor change in the general shape of the Arrhenius plots for the different annealing steps. The lines for E(0.1) and E(0.2) in Fig. 7 are drawn to justify the energy range given in Table II rather than to suggest that they are a combination of exactly two separate levels.

E. Tentative identification of the deep levels observed

An energy state with similar signatures as H(0.37) has been reported previously by Zettler *et al.*[11] in ITO/Si. The shape of the H(0.37) peak resembles that expected theoretically for a single level, and it arises most likely from a well-defined point defect. Considering the energy position of H(0.37), its

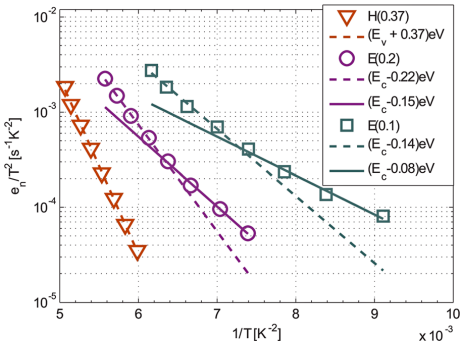

FIG. 7. (Color online) Arrhenius plot for the three dominant peaks, E(0.1)(120 °C), E(0.2)(250 °C anneal), and H(0.37)(120 °C anneal), seen in Fig. 6.

thermal stability, the high concentration of C and O at the ITO/Si interface, together with the use of Cz-Si wafers (oxygen concentration of about 10^{17} cm^{-3}), the interstitial-carbon interstitial-oxygen complex (C_iO_i) appears as a strong candidate.[21–25]

Indeed, C_iO_i is a dominant center in oxygen- and carbon-rich Si, subjected to irradiation with energetic particles (electrons, neutrons, and ions) and is very likely to form during the sputter-deposition process of the ITO films. H(0.37) starts to decrease in strength already at 200 °C in the present samples, while normally temperatures above 300 °C are required to loose C_iO_i centers.[25] However, C_iO_i interacts with other defects and impurities, like H, if they are present with sufficient concentration and the apparent stability of C_iO_i decreases.[26–28] Accordingly, as the SIMS measurements reveal a clear peak of H at the interface, the low stability of H(0.37) in the present samples is attributed to H-passivation of C_iO_i.

The signatures of the electron traps observed (Fig. 6 and Table II) are close to those found by Kuwano *et al.*;[12] in Ref. 12, three main electron traps located ~0.10, ~0.19, and ~0.25 eV below E_c were detected in the vicinity of the ITO/Si interface. The peaks are broad and might contain several overlapping levels or a band of levels, which suggests extended (high-order) complexes or highly perturbed centers rather than isolated point defects. This is somewhat in contrast to the multitude of single levels reported by Zettler *et al.*[11] for both *n*- and *p*-type substrates, although they appear in the same energy range as the peaks observed in the present study and in Ref. 12. One of the most prominent irradiation-induced defects in O-rich silicon is the vacancy-oxygen (*VO*) center with a characteristic acceptor level at $\sim E_c - 0.18$ eV (see Ref. 29 and references therein), i.e., in the energy range where several of the peaks occur in Fig. 6(a). High order vacancy complexes, like the di-vacancy, di-vacancy-oxygen, tri-vacancy, and tri-vacancy-oxygen centers,[29–32] give also rise to acceptor levels at $\sim E_c - 0.20$ eV (double minus to single minus charge state transitions), but they should be accompanied by corresponding levels in the range ~0.40 to 0.46 eV below E_c (single minus to neutral transitions). In this latter energy range, only the minor E(0.5) peak is found, and hence, higher-order vacancy-related complexes can most likely be excluded. Further, Kuwano *et al.*[12] showed that treatment of the Si samples in hydrogen-plasma prior to deposition of ITO substantially reduces the amplitude of the DLTS peaks, providing evidence for passivation of defects with dangling Si bonds. In addition to *V*O, one candidate may be the so-called P_b center,[33] which occurs frequently at oxide/Si interfaces and exhibits Si dangling bond character, but further work is indeed needed for a more firm identification.

IV. CONCLUSION

The electronic properties of ITO/*p*-Si and ITO/*n*-Si heterojunctions have been investigated, and two hole traps at 0.32 and 0.37 eV above E_v and a broad band of electron traps at 0.1–0.2 eV below E_c are revealed. Disappearance at ~250 °C of the dominant hole trap, H(0.37), which is assigned to the C_iO_i defect, improves the ITO/*p*-Si junction rectification, while annealing above 400-450 °C yields an Ohmic behavior between ITO and *p*-Si. The dominate electron traps disappear at 450–550 °C, resulting in a sharp increase in rectification of the ITO/*n*-Si junction. Hence, a clear correlation between annealing of the dominant electron traps and improved IV characteristics is observed. The identity of the electron traps is not fully established, but they involve centers with dangling bonds, and complexes containing *V*O- and P_b-like defect structures are possible candidates.

[1] A. Ashok, P. P. Sharma, and S. J. Fonash, IEEE Trans. Electron. Devices **27**, 725 (1980).
[2] H. Kobayashi, T. Ishida, Y. Nakato, and H. Tsubomura, J. Appl. Phys. **69**, 1736 (1991).
[3] P. Malar, V. Vijayan, A. K. Tyagi, and S. Kasiviswanathan, Nucl. Instrum. Methods Phys. Res. B **229**, 406 (2005).
[4] P. Malar, B. C. Mohanty, A. K. Balamurugan, S. Rajagopalan, A. K. Tyagi, and S. Kasiviswanathan, Surf. Interface Anal. **37**, 281 (2005).
[5] A. Subrahmanyam and N. Balasubramanian, Semicond. Sci. Technol. **7**, 324 (1992).
[6] M. Tanaka, M. Taguchi, T. Matsuyama, T. Sawada, S. Tsuda, S. Nakano, H. Hanafusa, and Y. Kuwano, Jpn. J. Appl. Phys. **31**, 3518 (1992).
[7] T. Sawada, N. Terada, S. Tsuge, T. Baba, T. Takahama, K. Wakisaka, S. Tsuda, and S. Nakano, in *1994 IEEE First World Conference on Photovoltaic Energy Conversion*, 1994, Conference Record of the Twenty Fourth IEEE Photovoltaic Specialists Conference, Waikoloa, HI, 5-9 December 1994, Vol. 2.
[8] M. Taguchi, K. Kawamoto, S. Tsuge, T. Baba, H. Sakata, M. Morizane, K. Uchihashi, N. Nakamura, S. Kiyama, and O. Oota, Prog. Photovoltaics **8**, 503 (2000).
[9] T. H. Wang, E. Iwaniczko, M. R. Page, D. H. Levi, Y. Yan, V. Yelundur, H. M. Branz, A. Rohatgi, and Q. Wang, in Photovoltaic Specialists Conference, 2005. Conference Record of the Thirty-first IEEE, Orlando, FL, 3-7 January 2005, pp. 955-958.
[10] Y. Tsunomura, Y. Yoshimine, M. Taguchi, T. Baba, T. Kinoshita, H. Kanno, H. Sakata, E. Maruyama, and M. Tanaka, Sol. Energy Mater. Sol. Cells **93**, 670 (2009).
[11] J. T. Zettler, J. Bollmann, K. H. Heckner, and H. A. Klose, Phys. Status Solidi A **112**, 395 (1989).
[12] K. Kuwano and S. Ashok, Appl. Surf. Sci. **117**, 629 (1997).
[13] E. V. Monakhov, R. Balasundaraprabhu, N. Muthukumarasamy, and B. G. Svensson, Mater. Sci. Eng., B **159**, 314 (2009).
[14] R. Balasundaraprabhu, E. V. Monakhov, N. Muthukumarasamy, O. Nilsen, and B. G. Svensson, Mater. Chem. Phys. **114**, 425 (2009).
[15] B. G. Svensson, K. H. Rydén, and B. M. S. Lewerentz, J. Appl. Phys. **66**, 1699 (1989).
[16] J. George and C. S. Menon, Surf. Coat. Technol. **132**, 45 (2000).
[17] H. Kim, C. M. Gilmore, A. Piqué, J. S. Horwitz, H. Mattoussi, H. Murata, Z. H. Kafafi, and D. B. Chrisey, J. Appl. Phys. **86**, 6451 (1999).
[18] T. Maruyama and K. Fukui, J. Appl. Phys. **70**, 3848 (1991).
[19] E. Terzini, P. Thilakan, and C. Minarini, Mater. Sci. Eng., B **77**, 110 (2000).
[20] A. B. Chebotareva, G. G. Untila, T. N. Kost, S. Jørgensen, and A. G. Ulyashin, Thin Solid Films **515**, 8505 (2007).
[21] G. Davies and R. C. Newman, Handbook in Semiconductors, edited by T. Moss and S. Mahajan (Elsevier, Amsterdam, 1994), Chap 21, p. 1557.
[22] P. M. Mooney, L. J. Cheng, M. Süli, J. D. Gerson, and J. W. Corbett, Phys. Rev. B **15**, 3836 (1977).
[23] J. M. Trombetta and G. D. Watkins, Appl. Phys. Lett. **51**, 1103 (1987).
[24] R. Jones and S. Öberg, Phys. Rev. Lett. **68**, 86 (1992).
[25] B. G. Svensson and J. L. Lindström, Phys. Status Solidi A **95**, 537 (1986).
[26] O. V. Feklisova, N. A. Yarykin, E. B. Yakimov, and J. Weber, Physica B **273**, 235 (1999).
[27] H. Malmbekk, L. Vines, E. V. Monakhov, and B. G. Svensson, Phys. Status Solidi C **8**, 705 (2011).
[28] S. Fatima, C. Jagadish, J. Lalita, B. G. Svensson, and A. Hallen, J. Appl. Phys. **85**, 2562 (1999).
[29] B. G. Svensson, EMIS Data Rev. Ser. **20**, 763 (1999).
[30] E. V. Monakhov, B. S. Avset, A. Hallén, and B. G. Svensson, Phys. Rev. B **65**, 233207 (2002).
[31] M. Mikelsen, E. V. Monakhov, G. Alfieri, B. S. Avset, and B. G. Svensson, Phys. Rev. B **72**, 195207 (2005).
[32] V. P. Markevich, A. R. Peaker, S. B. Lastovskii, L. I. Murin, J. Coutinho, V. J. B. Torres, P. R. Briddon, L. Dobaczewski, E. V. Monakhov, and B. G. Svensson, Phys. Rev. B **80**, 235207 (2009).
[33] E. H. Poindexter, G. J. Gerardi, M. E. Rueckel, P. J. Caplan, N. M. Johnson, and D. K. Biegelsen, J. Appl. Phys. **56**, 2844 (1984).